

Emergent order in hydrodynamic spin lattices

<https://doi.org/10.1038/s41586-021-03682-1>

Received: 6 July 2020

Accepted: 1 June 2021

Published online: 4 August 2021

 Check for updates

Pedro J. Sáenz^{1,2}, Giuseppe Pucci^{2,3}, Sam E. Turton², Alexis Goujon^{2,4}, Rodolfo R. Rosales², Jörn Dunkel² & John W. M. Bush²

Macroscale analogues^{1–3} of microscopic spin systems offer direct insights into fundamental physical principles, thereby advancing our understanding of synchronization phenomena⁴ and informing the design of novel classes of chiral metamaterials^{5–7}. Here we introduce hydrodynamic spin lattices (HSLs) of ‘walking’ droplets as a class of active spin systems with particle–wave coupling. HSLs reveal various non-equilibrium symmetry-breaking phenomena, including transitions from antiferromagnetic to ferromagnetic order that can be controlled by varying the lattice geometry and system rotation⁸. Theoretical predictions based on a generalized Kuramoto model⁴ derived from first principles rationalize our experimental observations, establishing HSLs as a versatile platform for exploring active phase oscillator dynamics. The tunability of HSLs suggests exciting directions for future research, from active spin–wave dynamics to hydrodynamic analogue computation and droplet-based topological insulators.

Broken-mirror symmetry is an essential feature of many physical and biological systems, from magnetic metals and composites⁹ to DNA¹⁰. The most fundamental manifestation of a broken left–right symmetry are the spins of elementary particles such as photons or electrons¹¹. Microscopic spin systems and their macroscopic analogues^{1,2} are attracting increasing interest^{12,13} as building blocks of information storage¹⁴ and metamaterials^{3,15} devices. Over the last decade, experimental realizations of ultracold fermionic lattice gases^{16,17} have spurred advances in the understanding of charge and spin transport, promising novel technological platforms for quantum computation^{18,19} and spintronics²⁰. In parallel, recent progress in the control of natural and artificial active matter has led to the discovery of emergent collective spin states in chemical^{21,22}, biological^{23–25} and synthetic²⁶ suspensions, inspiring the invention of chiral active metamaterials⁷. Here we demonstrate a class of HSL systems²⁷ that combines active self-propulsion and particle-wave dynamics.

An HSL consists of an array of in-phase bouncing droplets²⁸, each drop confined by a submerged circular well and orbiting on the surface of a vertically vibrated liquid bath (Fig. 1a, b; Supplementary Video 1). Despite being macroscopic classical objects, these ‘walking’ droplets display wave-mediated self and pair interactions reminiscent of those arising in microscopic systems²⁹. To demonstrate the tunability of HSLs, we induce a range of collective ‘magnetic’ ordering phenomena through variations in the vibrational forcing and lattice geometry, and by mimicking the effect of an applied magnetic field through imposition of system rotation⁸. We explain the experimentally observed particle–wave dynamics by deriving a mapping onto a reduced oscillator network description^{4,30}, generalizing models used to describe neuronal networks³¹ and other synchronization phenomena^{32,33}. This mapping establishes HSLs as a versatile platform for investigating

chiral symmetry breaking and synchronization phenomena far from equilibrium.

In our experiments, both the droplets and underlying liquid bath consist of the same 20 centistokes (cSt) silicon oil (1 cSt = 1 mm² s^{−1}; Methods section ‘Experiments’). An electromagnetic shaker vibrates the bath vertically with forcing acceleration $F(t) = \gamma \cos(2\pi ft)$, where γ is the maximum acceleration, f the oscillation frequency, and t time (Fig. 1b). For sufficiently strong acceleration, the air layer between the drop and bath prevents direct contact, thus enabling persistent bouncing³⁴. When the drop bounces at half the driving frequency—and so achieves resonance with the bath’s most unstable wave mode—it excites radially decaying circular waves of characteristic wavelength λ_f on the bath surface^{34–36}. The amplitude and spatio-temporal decay of these waves can be controlled through the driving³⁵. When the driving amplitude γ is increased beyond a critical walking threshold γ_w , vertical bouncing becomes unstable and transitions to horizontal walking^{29,34}. As walking droplets land on the slopes of the underlying wave field η , they experience a wave-induced horizontal force $\mathbf{F}_i(\mathbf{x}_i, t) \propto -\nabla\eta|_{\mathbf{x}=\mathbf{x}_i}$, proportional to the wave slope $\nabla\eta$ at the point of impact $\mathbf{x}_i(t)$. Free droplets thus walk at constant speed along straight lines when $\gamma > \gamma_w$ (ref. ³⁴).

To transform linear motion into circular motion, we confined each walker to a submerged circular well³⁷ (Fig. 1b, Methods section ‘Experiments’). The resulting clockwise or anticlockwise motions were characterized by measuring the specific spin $S(t) = L_z(t)/m$, where m is the droplet’s mass and L_z denotes its angular momentum with respect to the well centre. Spin is thus understood in classical terms as corresponding to orbital motion. We first quantified how the spin of an isolated walker depends on the driving strength by progressively increasing the forcing acceleration γ towards the Faraday threshold γ_F , at which the bath surface becomes unstable in the absence of droplets^{35,36}. These

¹Department of Mathematics, University of North Carolina, Chapel Hill, NC, USA. ²Department of Mathematics, Massachusetts Institute of Technology, Cambridge, MA, USA. ³Institut de Physique de Rennes, CNRS, Université de Rennes, UMR 6251, Rennes, France. ⁴School of Engineering, École Polytechnique Fédérale de Lausanne, Lausanne, Switzerland. [✉]e-mail: saenz@unc.edu; bush@math.mit.edu

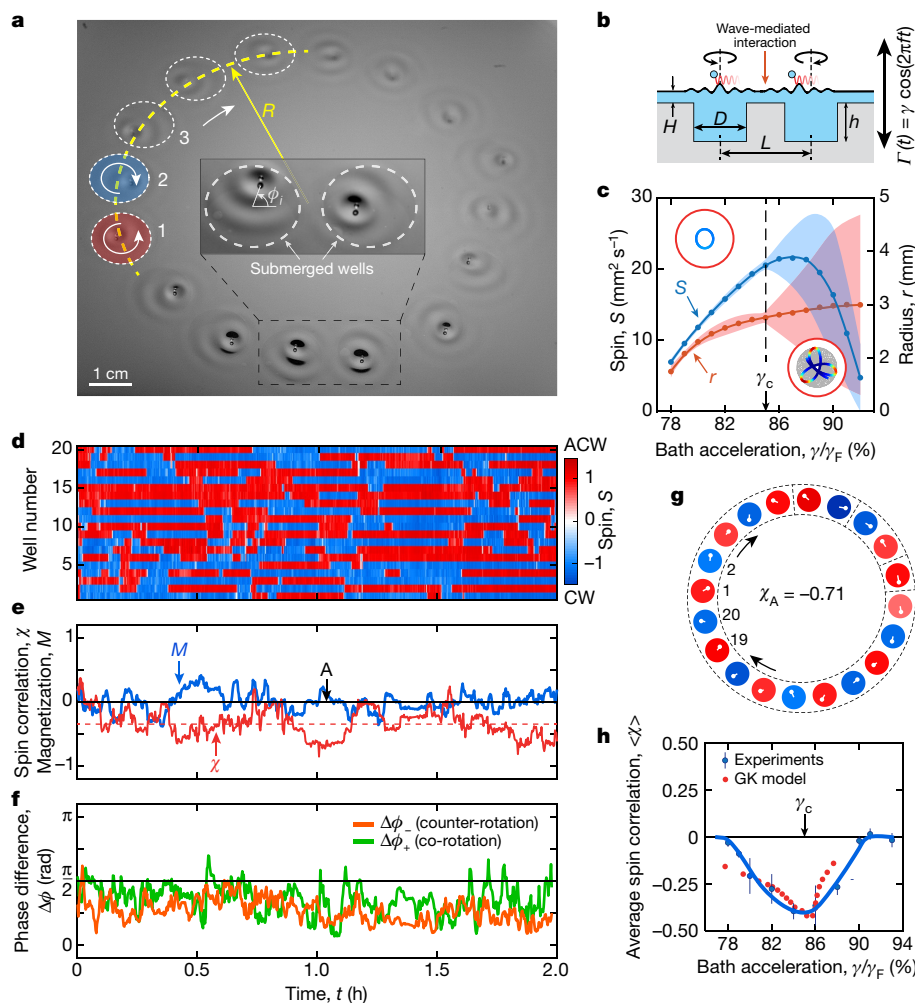


Fig. 1 | Spontaneous antiferromagnetic order in a 1D HSL. **a, b**, Oblique view (**a**) and schematic cross section (**b**) of a ring (of radius R) of submerged circular wells (of diameter D , depth H , centre separation L), each containing a single drop executing clockwise or anticlockwise motion on the surface of a vibrating fluid bath. A thin fluid layer (of depth h) between wells enables wave-mediated interactions between neighbouring droplets (Supplementary Video 1). **c**, Dependence of the spin S and orbital radius r of an isolated walker ($D=14$ mm, $H=1$ mm, $f=80$ Hz) on the dimensionless bath acceleration γ/γ_F . The solid lines are fits resulting from smoothing the piecewise linear curve obtained by connecting the data points. Once γ exceeds a critical threshold γ_c , the drop's circular trajectory destabilizes into a precessing trefoil, increasing spin variation and susceptibility to perturbation-induced spin flips. For a given driving acceleration, only one state is observed. Insets, two typical drop trajectories, coloured by their instantaneous spin value, at low (top left) and high (bottom right) accelerations. Centrelines denote interpolated mean values and envelopes indicate standard deviations. **d–f**, Temporal evolution of the spin values S_i (**d**), spin pair correlation χ and magnetization M (**e**), and phase difference $\Delta\phi$ (**f**) for a 1D periodic HSL with $N=20$ wells driven at $\gamma/\gamma_F=82.0\%$. **g**, Snapshot showing collective antiferromagnetic order at instant A in **e** (Supplementary Video 2). χ_A is the spin–spin correlation χ at instant A in **e**. Dashed lines highlight domains of local antiferromagnetic order. White circles mark drop positions, background colour shows the spin magnitude. **h**, Dependence of the average spin correlation ($\langle\chi\rangle$) on γ/γ_F . Solid lines are fits resulting from smoothing the piecewise linear curve obtained by connecting the data points as in **c**. The average spin correlation ($\langle\chi\rangle$) indicates maximal antiferromagnetic ordering for $\gamma\approx\gamma_c$, highlighting that stable single-spin trajectories promote collective ordering. Error bars denote the standard deviations (Methods section ‘Statistics’). Experimental parameters in **d–h**: $L=17.7$ mm, $D=14$ mm, $H=1$ mm, $N=20$, $f=80$ Hz, $\gamma_F=4.780g$ (where g is the gravitational acceleration), $\lambda_F=4.75$ mm. ACW, anticlockwise; CW, clockwise.

single-spin measurements revealed an optimal signal-to-driving ratio for $S(t)$ at a vibrational acceleration $\gamma_c \approx 0.85\gamma_F$ (Fig. 1c). For suboptimal driving $\gamma < \gamma_c$, the mean spin decreases with the walker's characteristic speed as γ decreases³⁶. For $\gamma > \gamma_c$, the circular orbits deform into precessing trefoils (Fig. 1c) that exhibit a larger spin variance, making them more susceptible to spin flips when perturbed. Armed with this understanding of the single-spin states, we investigated the collective spin dynamics in one-dimensional (1D) and two-dimensional (2D) HSLs.

The wave-mediated spin–spin coupling in HSLs is reminiscent of spatially oscillating interactions^{9,38} in Ruderman–Kittel–Kasuya–Yosida (RKKY)-type spin models. Our experimental setup allowed us to tune the magnitude of the spin–spin coupling by varying the driving acceleration γ and the depth H of the fluid bath between adjacent wells (Fig. 1b; Methods section ‘Experiments’). When the pair coupling is sufficiently strong, nearest-neighbour interactions may cause spin flips. To determine whether such flips can facilitate coherent collective dynamics across the lattice, we measured the normalized effective ‘magnetization’ $M(t) = \sum_i S_i(t)$ and spin–spin correlation $\chi(t) = \sum_{i,j} S_i(t)S_j(t)$, where $\sum_{i,j}$ denotes a sum over adjacent pairs. To achieve statistical significance, experiments were run for several hours: in 1 h a droplet performs approximately 10^5 bounces and approximately 1,800 orbits (Methods section ‘Statistics’). Positive values of χ signal parallel alignment of neighbouring spins (‘ferromagnetic’ order) whereas negative values of χ indicate antiparallel alignment (‘antiferromagnetic’ order).

The oscillatory wave-mediated spin–spin coupling suggests that HSLs can support different types of collective order depending on the ratio between lattice spacing L and Faraday wavelength λ_F . To test this hypothesis, we studied a 1D periodic (circular) HSL with $N=20$ equally spaced wells and $L/\lambda_F=3.7$ (Fig. 1a, d–h). Starting from a random initial spin configuration (Methods section ‘Statistics’), we observed that pair interactions can trigger multiple spin flips (Fig. 1d), leading to fluctuations in the instantaneous magnetization and spin–spin correlation (Fig. 1e). The magnetization vanishing on average, $\langle M \rangle \approx 0$, indicated that global mirror symmetry was preserved (Fig. 1e). However, the negative pair correlation, $\langle \chi \rangle < 0$, revealed a bias towards local antiferromagnetic order (Fig. 1g; Supplementary Video 2). Holding L/λ_F fixed, a similar antiferromagnetic bias occurred in experiments with non-periodic boundary conditions, different N values, and different lattice radii R (Methods section ‘Statistics’), confirming that antiferromagnetic ordering is selected by the lattice spacing. The strength of the emergent antiferromagnetic order depends non-monotonically on the driving amplitude γ (Fig. 1h; Methods section ‘Statistics’). The strongest collective antiferromagnetic response was observed for $\gamma \approx \gamma_c$, indicating a correlation between the global collective ordering and the robustness of a single spin state (Fig. 1c).

The emergence of local magnetic ordering can be understood by analysing the drops' horizontal phase ϕ_i , which plays a role analogous to the polar angle in XY -type spin models (Fig. 1a). To quantify pairwise

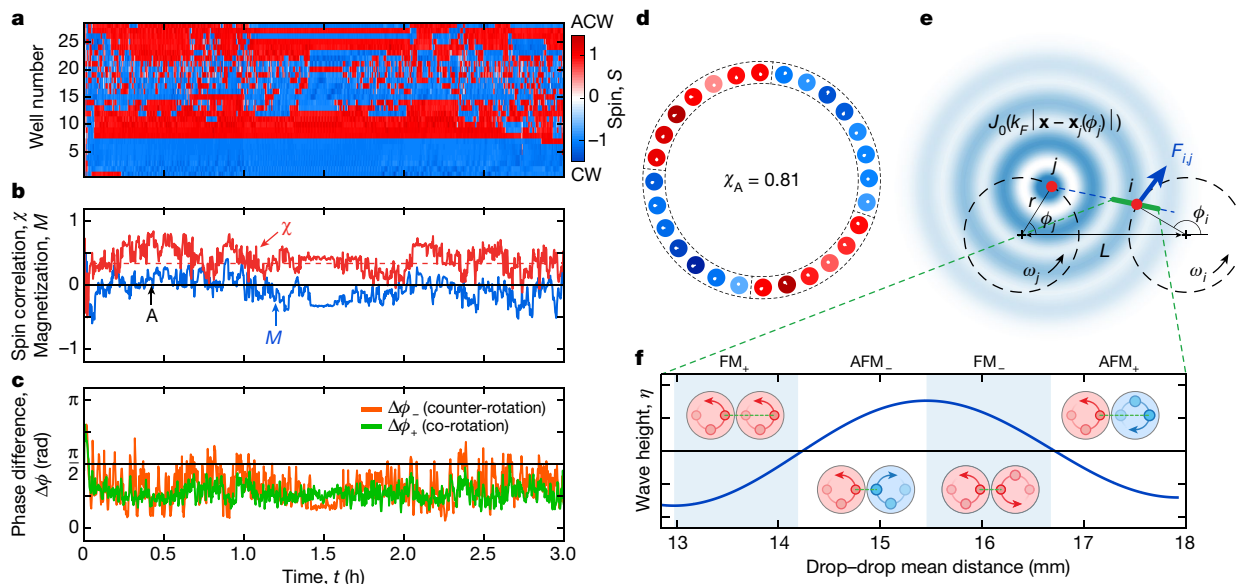


Fig. 2 | Tuning collective order through the lattice parameters in experiments and theory. When the lattice spacing is reduced to $L = 13.2$ mm, the 1D HSL spontaneously settles into ferromagnetic order. Parameters: $D = 10$ mm, $H = 0.8$ mm, $N = 28$, $f = 78$ Hz, $\gamma/\gamma_f = 86.0\%$, $\gamma_f = 5.280g$, $\lambda_f = 4.84$ mm. **a–c**, The preferred local ferromagnetic order is reflected in the instantaneous spins S_i (**a**), spin–spin correlation χ and magnetization M (**b**), and the mean phase differences $\Delta\phi_{\pm}$ (**c**). **d**, Spin configuration at instant A in **b** showing four domains of ferromagnetic order (Supplementary Video 3). **e**, Geometry considered in the theoretical wave model. Neighbouring drops i and j move

along circular trajectories of radius r at angular speed $\pm\omega$. The drop position is determined by the angular phase ϕ , defined with respect to the lattice centreline. Drop i is subject to a force F_{ij} along its direction of motion, owing to the wave field generated by drop j , as is approximated by a Bessel function J_0 centred at its position. **f**, Depending on the drop separation, four dominant drop-pair synchronization modes are favoured, leading to the emergence of alternating ferromagnetic and antiferromagnetic local order as the lattice spacing is varied (Methods section ‘Simulations’). ACW, anticlockwise; CW, clockwise.

phase synchronization, we recorded the mean phase differences $\Delta\phi_{\pm}$ for co-rotating (+) and counter-rotating (–) neighbouring pairs, respectively (see Methods section ‘Statistics’). These observables signal in-phase ($\Delta\phi_{\pm} \rightarrow 0$) or out-of-phase ($\Delta\phi_{\pm} \rightarrow \pi$) rotations of neighbouring walkers, and so also indicate their relative distance. For antiferromagnetic HSLs, we found a substantial bias towards in-phase rotations (Fig. 1f). In particular, both spin–spin correlation (Fig. 1h) and phase synchronization are maximized at driving strength $\gamma \approx \gamma_c$, implying a causal link between coherent orbital synchronization and emergent spin order.

To demonstrate how the collective spin dynamics depends on lattice geometry, we performed 1D experiments for a reduced lattice spacing $L/\lambda_f = 2.8$ (Fig. 2a–d). The resulting changes in the wave-mediated spin interactions (Fig. 2e) support extended domains of ferromagnetic ordering, as reflected by a positive pair correlation, $\langle\chi\rangle > 0$ (Fig. 2b, d; Supplementary Video 3), with a bias towards in-phase rotation (Fig. 2c). As in the antiferromagnetic HSL with $L/\lambda_f = 3.7$, we observed no global magnetization, $\langle M \rangle \approx 0$, indicating that changes in lattice geometry can be used to control local magnetic order but do not lead to global mirror-symmetry breaking.

To rationalize the manner in which geometry dictates collective spin order and phase synchronization in HSLs, we derived a generic phase oscillator model from a detailed hydrodynamic description of our experimental system (Fig. 2e; Methods section ‘Theory’). In this model, we focus on subcritical driving $\gamma \leq \gamma_c$ (Fig. 1c), so that each walker i follows a circular trajectory $\mathbf{x}_i(t) = r_0(\cos\phi_i(t), \sin\phi_i(t))$, with angular frequency $\omega_i = \dot{\phi}_i$, where (r_0, ϕ_i) are the cylindrical coordinates with respect to the centre of each well. The walking speed v_0 then defines a preferred orbital frequency $\pm\omega_0 = \pm v_0/r_0$ (ref. ³⁶). Modelling this effect by a nonlinear Rayleigh-type friction, the phase dynamics of a walker is described by

$$\dot{\omega}_i = \frac{1}{\tau} \left(1 - \frac{\omega_i^2}{\omega_0^2} \right) \omega_i + \sum_j F_{ij}(\phi_i, \phi_j). \quad (1)$$

Equation (1) can be interpreted as an active XY-type model⁹, in which perturbations to ω_0 decay over the timescale τ , and F_{ij} is the wave-mediated force exerted on drop i by its nearest neighbour j (Fig. 2e). For weak accelerations and small orbital radii $r_0 \ll L$, the interaction force $F_{ij}(\phi_i, \phi_j) = -\partial U/\partial\phi_i$ can be derived from the effective coupling potential $U(\phi_i, \phi_j) = \frac{1}{2}\alpha(\cos\phi_i - \cos\phi_j)^2 + \frac{1}{2}\beta(\sin\phi_i - \sin\phi_j)^2$ (Methods section ‘Theory’). The coefficients are proportional to the curvature, $\alpha \propto J_0''(k_f L)$, and gradient, $\beta \propto J_0'(k_f L)$, of the coupling wave field, which is well approximated by a Bessel function of the first kind $J_0(k_f|\mathbf{x} - \mathbf{x}_j|)$ centred at the neighbouring drop position. Here prime symbols denote derivatives with respect to $r_j = |\mathbf{x} - \mathbf{x}_j|$, and $k_f = 2\pi/\lambda_f$ the Faraday wave-number. HSLs characterized by purely circular orbits, as arise for $\gamma \leq \gamma_c$, thus belong to a generalized Kuramoto universality class⁴.

Analysis of the phase-oscillator dynamics (equation (1)) confirms that the spin–spin correlation alternates between ferromagnetic and antiferromagnetic order as the lattice spacing L is varied (Extended Data Fig. 4a). The associated mean phase differences (Extended Data Fig. 4b) revealed four different modes of pairwise symmetry breaking. Specifically, there are two ferromagnetic phases FM_{\pm} and two antiferromagnetic phases AFM_{\pm} , distinguished by preferential in-phase (+) and out-of-phase (–) rotation, respectively (Fig. 2f). Depending on L , the force parameters α and β can be either positive or negative, yielding four magnetic phases corresponding to minima of the coupling potential. The model predictions agree well with our experimental data: the antiferromagnetic (Fig. 1d–f; $L = 17.7$ mm) and ferromagnetic (Fig. 2a–c; $L = 13.2$ mm) HSL experiments fall within the predicted AFM_{+} and FM_{+} ranges, respectively. The theory also captures how the preferred order varies with vibrational acceleration (Fig. 1h, Extended Data Fig. 5).

The spins in an antiferromagnetic material may be realigned into a ferromagnetic state by imposing a constant magnetic field \mathbf{B} (ref. ⁹). We next sought to determine whether HSLs can undergo similar global symmetry breaking. The Lorentz force $\mathbf{F}_B = q(\mathbf{v} \times \mathbf{B})$ acting on a charge q

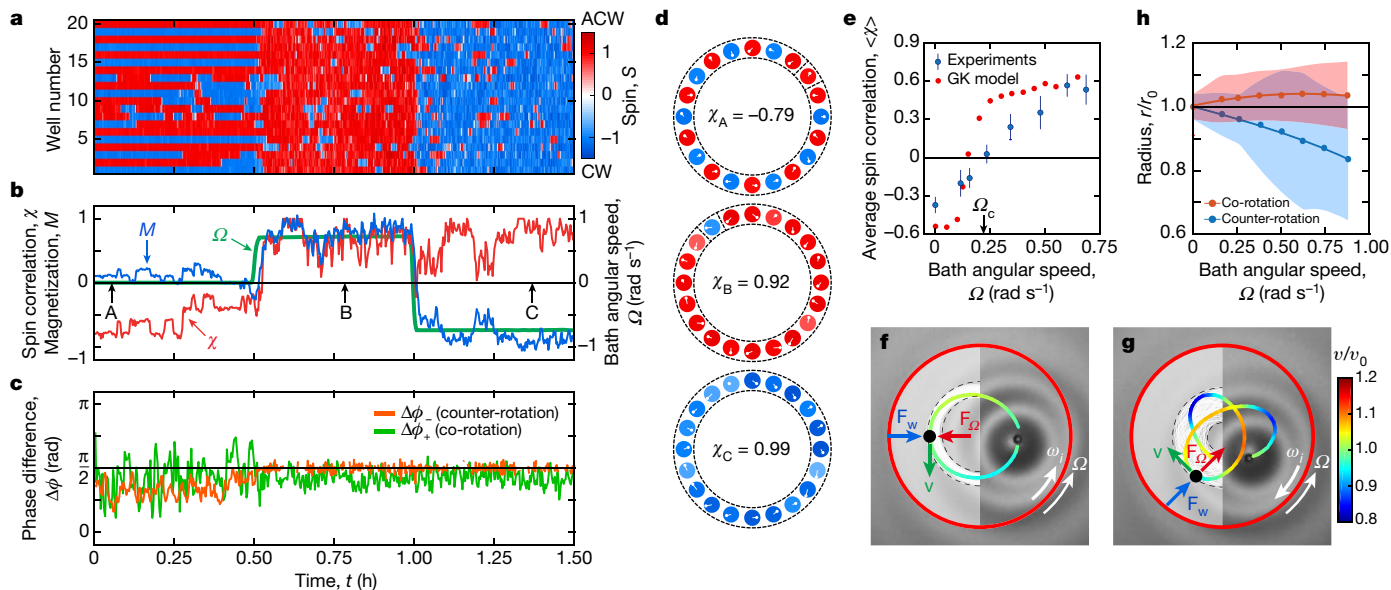


Fig. 3 | Inducing global polarization through applied rotation. Rotating the circular HSL from Fig. 1d–h induces a transition from effective antiferromagnetic to ferromagnetic order. **a–c**, The experiment was run for 1 h without rotation before the recording process started. During the first 0.5 h of data acquisition, the experiment continued without rotation ($\Omega = 0$) with the HSL exhibiting local antiferromagnetic order with no net magnetization. At $t = 0.5$ h, the bath rotation was switched on ($\Omega = 0.7 \text{ rad s}^{-1}$, anticlockwise) inducing a transition to ferromagnetic order and positive magnetization. At $t = 1$ h, the rotation direction was reversed ($\Omega = -0.7 \text{ rad s}^{-1}$, clockwise), leading to negative magnetization. Lattice parameters and forcing frequency are the same as in Fig. 1 and $\gamma \approx \gamma_c$. **d**, Instantaneous spin configurations at time points A–C in **b**, showing antiferromagnetic and ferromagnetic ordering (Supplementary Video 4).

χ_A, χ_B and χ_C are the spin–spin correlations at instants A, B and C. **e**, Average spin correlation ($\langle \chi \rangle$) signals a transition to ferromagnetic order at $\Omega_c \approx 0.22 \text{ rad s}^{-1}$ (Methods section ‘Statistics’). **f, g**, Force balance and measured trajectory, colour-coded by speed, for an isolated spin in a frame co-rotating with the bath. The drop’s trajectory is nearly circular when its angular velocity ω and the bath rotation Ω are aligned, but approximates a precessing trefoil when the signs are opposite. **h**, Mean orbital radius r versus bath angular speed Ω for a walker co-rotating and counter-rotating with respect to the bath, as in **f** and **g**, respectively; r_0 is the trajectory radius for $\Omega = 0$ shown in Fig. 1c. Solid lines are fits resulting from smoothing the piecewise linear curve obtained by connecting the data points as in Fig. 1. The centre line denotes the mean radius, and the envelope indicates the standard deviation. ACW, anticlockwise; CW, clockwise.

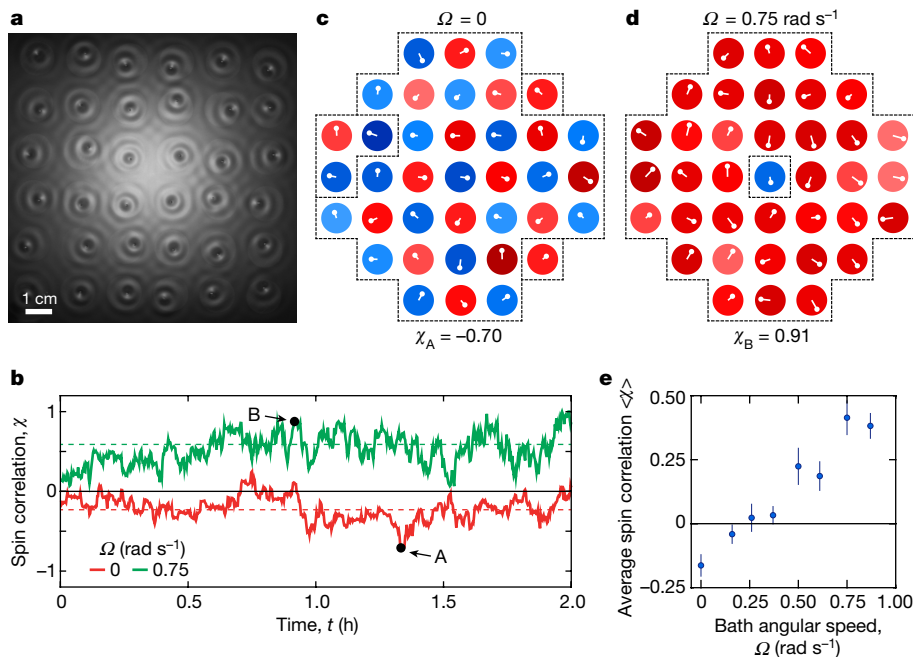


Fig. 4 | Rotation-induced polarization transition from antiferromagnetic to ferromagnetic order in 2D square lattices. **a**, Top view showing the wave field of a square lattice with $L = 17.3 \text{ mm}$, $D = 13 \text{ mm}$, $H = 0.96 \text{ mm}$, $f = 80 \text{ Hz}$, $\gamma/\gamma_f = 86\%$ and $\gamma_f \approx 4.940g$. **b**, Evolution in time of the spin correlation χ reveals preferred antiferromagnetic order for a stationary lattice ($\Omega = 0$), and

ferromagnetic order for a rotating lattice ($\Omega = 0.75 \text{ rad s}^{-1}$). **c, d**, Instantaneous spin arrangements at time points A and B in **b**, showing the emergence of antiferromagnetic (**c**), and ferromagnetic (**d**) domains, respectively (Supplementary Video 5). **e**, A transition from antiferromagnetic to ferromagnetic order is prompted by increasing the bath’s angular speed.

moving with velocity \mathbf{v} has precisely the same form as the Coriolis force $\mathbf{F}_\Omega = m(\mathbf{v} \times 2\boldsymbol{\Omega})$ acting on a mass m moving with velocity \mathbf{v} in a frame rotating at constant angular velocity $\boldsymbol{\Omega}$ (ref. ⁸). This suggests the possibility of transforming antiferromagnetic HSLs into ferromagnetic states by rotating the vibrating bath about a vertical axis at a rate Ω (Methods section ‘Experiments’). To test this hypothesis, we initialized the antiferromagnetic HSL described in Fig. 1 without bath rotation ($\Omega = 0$) and let it equilibrate for 1 h. Keeping $\Omega = 0$ for another 0.5 h, the HSL remained in the antiferromagnetic state as expected (Fig. 3a, b; $t < 0.5$ h). At $t = 0.5$ h, we began to rotate the setup anticlockwise by gradually increasing the rotation rate to $\Omega = 0.7$ rad s^{-1} . In a matter of seconds, most spins had co-aligned with the bath rotation, leading to a strongly positive spin correlation, $\langle \chi \rangle \approx 0.58$. However, unlike the steady HSL in Fig. 2a–d, the rotated HSL had a net magnetization, $\langle M \rangle \approx 0.78$. Moreover, when the rotation direction was reversed to $\Omega = -0.7$ rad s^{-1} (clockwise) at $t = 1$ h, most of the spins flipped to realign with the inverted ‘magnetic’ field. The effective magnetization thus became negative, $\langle M \rangle < 0$, while the spin pairs remained ferromagnetically arranged, $\langle \chi \rangle > 0$ (Fig. 3b; Supplementary Video 4). The transition to ferromagnetic order requires a supercritical rotation rate $|\Omega| > \Omega_c \approx 0.22$ rad s^{-1} (Fig. 3e). Rotation also affects the pairwise phase synchronization: as the spin dynamics become dominated by the Coriolis force, the phase differences become uncorrelated, thus averaging to the mean $\langle \Delta\phi_{ij} \rangle \approx \pi/2$ (Fig. 3c).

Examining the single-spin dynamics in the rotating frame reveals the mechanism responsible for the field-induced polarization (Fig. 3f, g). For optimal driving, $\gamma \approx \gamma_c$, a walker executes circular motion in the absence of rotation (Fig. 1c). When rotation is switched on, a drop co-orbiting with the bath experiences a Coriolis force \mathbf{F}_Ω that opposes the confining force of the submerged well \mathbf{F}_w (ref. ³⁷) (Fig. 3f). As a result, the drop preserves its circular trajectory but its orbital radius increases with Ω (Fig. 3h). Conversely, when the walker is counter-rotating with respect to the bath, both \mathbf{F}_w and \mathbf{F}_Ω point inwards (Fig. 3g), destabilizing the circular orbits into trefoil-like trajectories similar to those observed for $\Omega = 0$ and $\gamma > \gamma_c$ (Fig. 1c). Droplets on these trefoil-like trajectories pass closer to the well centres (Fig. 3h), where their walking directions can be more easily reversed by perturbations from their neighbours. Hence, confinement favours co-rotating orbits in HSLs; conversely, free walkers prefer counter-rotating inertial orbits⁸. We note that a generalization of our phase-oscillator model captures the effects of the external field (Fig. 3e; Methods section ‘Theory’).

Two-dimensional classical and quantum spin lattices display features that are absent in their 1D counterparts, including geometric frustration and topological order⁹. HSLs provide a promising platform for exploring such effects at the macroscale. For example, square HSLs (Fig. 4a; Supplementary Video 5) that promote antiferromagnetic order in the absence of rotation ($\Omega = 0$; Fig. 4b, c), undergo a polarization transition ($\Omega > 0$; Fig. 4b, d) as the Coriolis force is increased (Fig. 4e). Additionally, simulations of larger lattices confirm the emergence of collective magnetic order in square lattices (Extended Data Fig. 6).

To conclude, since lattice geometry (Extended Data Fig. 7) and the interactions between lattice sites can be directly tailored in various ways (Methods section ‘Tunability’), we expect HSLs to provide a versatile testbed for designing wave-coupled autonomous metamaterials³⁹, exploring active spin-wave dynamics¹³, and studying Anderson-type wave localization phenomena⁴⁰ far from equilibrium.

Online content

Any methods, additional references, Nature Research reporting summaries, source data, extended data, supplementary information, acknowledgements, peer review information; details of author contributions

and competing interests; and statements of data and code availability are available at <https://doi.org/10.1038/s41586-021-03682-1>.

- Kane, C. L. & Lubensky, T. C. Topological boundary modes in isostatic lattices. *Nat. Phys.* **10**, 39–45 (2014).
- Chen, B. G.-g., Upadhyaya, N. & Vitelli, V. Nonlinear conduction via solitons in a topological mechanical insulator. *Proc. Natl Acad. Sci. USA* **111**, 13004–13009 (2014).
- Nash, L. M. et al. Topological mechanics of gyroscopic metamaterials. *Proc. Natl Acad. Sci. USA* **112**, 14495–14500 (2015).
- Strogatz, S. H. From Kuramoto to Crawford: exploring the onset of synchronization in populations of coupled oscillators. *Physica D* **143**, 1–20 (2000).
- Rechtsman, M. C. et al. Optimized structures for photonic quasicrystals. *Phys. Rev. Lett.* **101**, 073902 (2008).
- van Zuijden, B. C. et al. Spatiotemporal order and emergent edge currents in active spinner materials. *Proc. Natl Acad. Sci. USA* **113**, 12919–12924 (2016).
- Soni, V. et al. The odd free surface flows of a colloidal chiral fluid. *Nat. Phys.* **15**, 1188–1194 (2019).
- Fort, E. et al. Path-memory induced quantization of classical orbits. *Proc. Natl Acad. Sci. USA* **107**, 17515–17520 (2010).
- Coey, J. M. D. *Magnetism and Magnetic Materials* (Cambridge Univ. Press, 2010).
- Watson, J. D. & Crick, F. H. C. The structure of DNA. *Cold Spring Harb. Symp. Quant. Biol.* **18**, 123–131 (1953).
- Weinberg, S. *The Quantum Theory of Fields* Vol. 2 (Cambridge Univ. Press, 1996).
- Baltz, V. et al. Antiferromagnetic spintronics. *Rev. Mod. Phys.* **90**, 015005 (2018).
- Chumak, A. V. et al. Magnon spintronics. *Nat. Phys.* **11**, 453–461 (2015).
- Maurer, P. C. et al. Room-temperature quantum bit memory exceeding one second. *Science* **336**, 1283–1286 (2012).
- Süsstrunk, R. & Huber, S. D. Observation of phononic helical edge states in a mechanical topological insulator. *Science* **349**, 47–50 (2015).
- Schneider, U. et al. Metallic and insulating phases of repulsively interacting fermions in a 3D optical lattice. *Science* **322**, 1520–1525 (2008).
- Cheuk, L. W. et al. Quantum-gas microscope for fermionic atoms. *Phys. Rev. Lett.* **114**, 193001 (2015).
- Bulut, I., Asshab, S. & Nori, F. Natural and artificial atoms for quantum computation. *Rep. Prog. Phys.* **74**, 104401 (2011).
- Gross, C. & Bloch, I. Quantum simulations with ultracold atoms in optical lattices. *Science* **357**, 995–1001 (2017).
- Dieny, B. et al. Opportunities and challenges for spintronics in the microelectronics industry. *Nat. Electron.* **3**, 446–459 (2020).
- Biktashev, V. N., Barkley, D. & Biktasheva, I. V. Orbital motion of spiral waves in excitable media. *Phys. Rev. Lett.* **104**, 058302 (2010).
- Totz, J. F. et al. Spiral wave chimera states in large populations of coupled chemical oscillators. *Nat. Phys.* **14**, 282–285 (2018).
- Wioland, H. et al. Ferromagnetic and antiferromagnetic order in bacterial vortex lattices. *Nat. Phys.* **12**, 341–345 (2016).
- Nishiguchi, D. et al. Engineering bacterial vortex lattice via direct laser lithography. *Nat. Commun.* **9**, 4486 (2018).
- Riedel, I. H., Kruse, K. & Howard, J. A self-organized vortex array of hydrodynamically entrained sperm cells. *Science* **309**, 300–303 (2005).
- Souslov, A. et al. Topological sound in active-liquid metamaterials. *Nat. Phys.* **13**, 1091–1094 (2017).
- Sáenz, P. J. et al. Spin lattices of walking droplets. *Phys. Rev. Fluids* **3**, 100508 (2018).
- Couder, Y. et al. Dynamical phenomena: walking and orbiting droplets. *Nature* **437**, 208 (2005).
- Bush, J. W. M. Pilot-wave hydrodynamics. *Ann. Rev. Fluid Mech.* **47**, 269–292 (2015).
- Lindner, B. et al. Effects of noise in excitable systems. *Phys. Rep.* **392**, 321–424 (2004).
- Cumin, D. & Unsworth, C. P. Generalising the Kuramoto model for the study of neuronal synchronization in the brain. *Physica D* **226**, 181–196 (2007).
- Matheny, M. H. et al. Exotic states in a simple network of nanoelectromechanical oscillators. *Science* **363**, eaav7932 (2019).
- Dörfler, F. & Bullo, F. Synchronization in complex networks of phase oscillators: a survey. *Automatica* **50**, 1539–1564 (2014).
- Protière, S., Boudaoud, A. & Couder, Y. Particle-wave association on a fluid interface. *J. Fluid Mech.* **554**, 85–108 (2006).
- Eddi, A. et al. Information stored in Faraday waves: the origin of a path memory. *J. Fluid Mech.* **674**, 433–463 (2011).
- Moláček, J. & Bush, J. W. M. Drops walking on a vibrating bath: towards a hydrodynamic pilot-wave theory. *J. Fluid Mech.* **727**, 612–647 (2013).
- Sáenz, P. J., Cristea-Platon, T. & Bush, J. W. M. A hydrodynamic analog of Friedel oscillations. *Sci. Adv.* **6**, eaay9234 (2020).
- Ruderman, M. A. & Kittel, C. Indirect exchange coupling of nuclear magnetic moments by conduction electrons. *Phys. Rev.* **96**, 99–102 (1954).
- Ronellenfitch, H. et al. Inverse design of discrete mechanical metamaterials. *Phys. Rev. Mater.* **3**, 095201 (2019).
- Legendijk, A., Van Tiggelen, B. & Wiersma, D. S. Fifty years of Anderson localization. *Phys. Today* **62**, 24 (2009).

Publisher’s note Springer Nature remains neutral with regard to jurisdictional claims in published maps and institutional affiliations.

© The Author(s), under exclusive licence to Springer Nature Limited 2021

Methods

Introduction

Walking droplets in free space self-propel in a rectilinear fashion^{28,34–36}. Hydrodynamic spin states⁴¹, in which a droplet executes circular orbits confined by its own wave field are generally thought to be unstable in the laboratory^{42,43}, unless confined by an external force such as a linear spring force⁴⁴ or the Coriolis force that acts in a rotating frame^{8,45–47}. Recent experiments have demonstrated that variable bottom topography may be exploited to realize new hydrodynamic quantum analogues^{37,48}; in particular, the influence of a submerged well has led to analogues of the so-called quantum mirage⁴⁸ and Friedel oscillations³⁷. In this work, we exploit variable bottom topography to stabilize a collection of interacting hydrodynamic spin states²⁷, and characterize the emergent collective order. We note that, although several works have considered the stability of stationary bouncing droplet lattices^{49–53}, and other works^{54,55} examined wave-induced correlations of walker pairs confined to adjacent 1D cavities, we present here a macroscopic analogue of electronic spin systems with large collections of orbiting droplets.

Experiments

Stationary bath. A schematic of the experimental setup is presented in Extended Data Fig. 1. A circular aluminium bath was filled with silicon oil with density $\rho = 950 \text{ kg m}^{-3}$, viscosity $\nu = 20.9 \text{ cSt}$, and surface tension $\sigma = 20.6 \text{ mN m}^{-1}$. The lattices of submerged wells were constructed by laser-cutting acrylic sheets of thickness $h = 6.2 \text{ mm}$, which were then bolted to the base of the bath. The well depth h was thus sufficiently large with respect to the Faraday wavelength, $\lambda_F < 5 \text{ mm}$, for the liquid inside the wells to be in the deep-water wave regime⁵⁶. Similarly, the minimum distance d between the bath's outer wall and the outermost well was sufficiently large, $d > 6\lambda_F$, to ensure that the meniscus waves⁵⁷ that originated at the bath wall had no effect on the experiments. We note that the Faraday wavelengths corresponding to the shallow λ_F^H and deep λ_F^h regions are only marginally different, specifically $\lambda_F^h/\lambda_F^H \approx 1.05$. For the sake of simplicity of notation, we thus simply refer to both wavelengths as λ_F .

The bath was mounted on an optical table (Newport SG-34-4 custom breadboard, $3.0' \times 4.0' \times 4.32''$) and vibrated vertically by an electromagnetic shaker (Data Physics, V55) with an external amplifier (Data Physics, PA300E) at acceleration $\Gamma(t) = \gamma \cos(\omega t)$, where γ and $f = \omega/2\pi$ are the maximum acceleration and frequency, respectively. The shaker is connected to the bath by a thin steel rod coupled with a linear air bearing (PIL.P., $4 \times 4''$ cross-section, $6.5''$ long hollow bar) that ensures a spatially uniform vibration to within 0.1% ⁵⁸. The forcing is monitored through a data-acquisition system (NI, USB-6343) with two piezoelectric accelerometers (PCB, 352C65), attached to the base plate on opposite sides of the drive shaft, and a closed-loop feedback ensures a constant acceleration amplitude to within $\pm 0.002g$ (ref. ⁵⁸); where g is the acceleration due to gravity. We define the Faraday threshold γ_F as the critical vibrational acceleration above which Faraday waves⁵⁹ appear above the wells. The experimental setup was left vibrating at $\gamma \approx \gamma_F$ for at least 1 h before running any experiment to ensure a steady state in the bath. The Faraday threshold was measured before and after each experimental run in order to ensure the constancy of the prescribed driving, γ/γ_F , which may drift slowly owing to weak variations in viscosity and surface tension resulting from ambient temperature changes. With this protocol, the standard day-to-day variation in γ_F was limited to $\pm 0.04g$, and the variation in each experimental run was limited to $|\Delta\gamma_F|/\gamma_F < 0.003$, where $\Delta\gamma_F$ represents the variation in the Faraday threshold over a 1-h segment.

Droplets of the same silicon oil with diameter $D_d = 0.75 \pm 0.01 \text{ mm}$ were generated with a piezoelectric droplet-on-demand generator⁶⁰, and placed manually above the submerged wells. The bath was illuminated with a LED light ring in order to increase the contrast between the drops and the black background. The motion of the droplets was

recorded at 19 frames per second with a CCD camera mounted directly above the bath, and tracked with an in-house particle-tracking algorithm written in Matlab. The form of the wave field was captured by recording the normal reflection of light at the free surface⁵⁷. To that end, a semi-reflective mirror at 45° was placed between the CCD camera and the bath, and the light ring was replaced by a diffuse-light lamp facing the mirror horizontally. One then observes images with bright regions corresponding to horizontal parts of the surface, extrema or saddle points⁵⁷. To ensure that ambient air currents did not affect the results, the vibrating bath was enclosed within a transparent acrylic chamber. Experimental results obtained using the acrylic chamber were compared to others in which the spin system was shielded by a transparent acrylic lid bolted directly to the top of the bath. We found that the effective noise in the system was slightly reduced with the lid, but that the emergent collective behaviour was statistically indistinguishable.

The experiments were performed with walking drops bouncing subharmonically³⁶ in resonance with the underlying Faraday wave field, each with the same vertical bouncing phase. To ensure in-phase bouncing, before each experiment the bath acceleration was reduced to $\gamma = 1.1g$, so that the droplets transitioned to harmonic bouncers³⁶, synchronized with the bath vibration. By observing the light reflected from the upper side of the droplets, which intensifies when the droplets deform during impact, we were able to deduce the vertical phase of all the drops instantaneously. We confirmed that the drops continued to bounce in phase when the driving acceleration was progressively increased beyond $\gamma = 1.1g$, and throughout the duration of the experiments. Switching in the vertical bouncing phase was observed only for driving accelerations, $\gamma/\gamma_F > 90\%$, beyond the acceleration range where coherent collective behaviour emerged (Fig. 1h).

Rotating bath. To subject hydrodynamic spin lattices to bulk rotation, we mounted the aluminium bath on a vertical shaft attached to the upper plate of the linear air bearing through a system of preloaded ball bearings. The freely rotating shaft was connected with a vibration damping coupling to a d.c. electric motor with a planetary gearbox (Phidgets, 12 V d.c. motor, 139:1 gearbox) housed inside the hollow air bearing (see Extended Data Fig. 1). The rotation rate was monitored with an optical rotary encoder (Phidgets, HKT22) and the electric motor controlled with an in-house Python programme, yielding a rotation rate Ω that was constant to within $\pm 2\%$.

The centrifugal force on the rotating bath induces a parabolic deformation of the fluid interface of the form

$$H_0(r) = H - \frac{\Omega^2 R_b^2}{4g} + \frac{\Omega^2}{2g} r^2, \quad (2)$$

where r is the radial coordinate with respect to the centre of the bath, H is the depth of the fluid at rest, and R_b the bath radius, which in the rotating experiments was $R_b = 88 \text{ mm}$ (Extended Data Fig. 1). To compensate for the parabolic shape of the fluid surface, the liquid volume was readjusted in experiments with periodic 1D lattices (Fig. 3) to ensure that $H_0(R) = 1 \text{ mm}$, where R is the radius of the annular ring (Fig. 1a). The resulting variation in depth across the wells did not exceed $40 \mu\text{m}$, and so had a negligible influence on the dynamics. While such an adjustment was not possible in experiments with 2D lattices, we note that for the relatively slow rotation rates required to induce the transition from antiferromagnetic to ferromagnetic order ($\Omega < 0.7 \text{ rad s}^{-1}$, Fig. 4e), the liquid height was reduced in the centre and increased in the periphery by $< 10\%$ with respect to the depth of fluid at rest.

Lattice parameters. The lattice parameters for the 1D antiferromagnetic lattice discussed in Fig. 1 are $L = 17.7 \text{ mm}$, $D = 14 \text{ mm}$, $H = 1 \text{ mm}$, $N = 20$, $f = 80 \text{ Hz}$, $\gamma_F = 4.780g$, $\lambda_F = 4.75 \text{ mm}$. The lattice parameters of the 1D ferromagnetic lattice shown in Fig. 2 are $L = 13.2 \text{ mm}$, $D = 10 \text{ mm}$, $H = 0.8 \text{ mm}$, $N = 28$, $f = 78 \text{ Hz}$, $\gamma_F = 5.280g$, $\lambda_F = 4.84 \text{ mm}$. We note that

Article

for the 1D ferromagnetic lattice, we reduced the well diameter D and liquid height H to compensate for the heightened pair coupling resulting from locating the wells closer to each other. Such modification helped reduce the effective noise by both increasing the wave damping in the shallow region, and stabilizing the droplets' circular trajectories. We note that the vibration frequency, which effectively sets the characteristic wavenumber k_f , was also fine-tuned to accentuate the ferromagnetic response. The lattice parameters for the 2D square lattice shown in Fig. 4 are $L = 17.3$ mm, $D = 13$ mm, $H = 0.96$ mm, $N = 37$, $f = 80$ Hz, $\gamma_f = 4.940g$, $\lambda_f = 4.75$ mm. Experiments were also performed with lattices with size $N = 7 \times 7$.

Statistics

Order parameters. To characterize the collective behaviour in HSLs, we define three instantaneous order parameters, specifically the magnetization $M(t)$, spin–spin correlation $\chi(t)$, and average phase difference $\Delta\phi(t)$. The magnetization, which serves to quantify the global symmetry breaking, is defined as

$$M(t) = \frac{\sum_i S_i(t)}{\sum_i |S_i(t)|}, \quad (3)$$

where \sum_i denotes the sum over all N spins, and $S_i(t) = L_{z,i}(t)/m$ is the specific spin of droplet i with mass m and angular momentum $L_{z,i}$ with respect to the well centre. The denominator is the normalizing factor such that $M \in [-1, 1]$. Positive (negative) values of $M(t)$ signal a larger number of walkers rotating anticlockwise (clockwise). Pairwise symmetry breaking is quantified through the normalized spin–spin correlation,

$$\chi(t) = \frac{\sum_{i,j} S_i(t)S_j(t)}{\sum_{i,j} |S_i(t)S_j(t)|}, \quad (4)$$

where $\sum_{i,j}$ denotes sums over pairs $\{i,j\}$ of adjacent walkers. $\chi \in [-1, 1]$ thus signals a preference for co-rotation ($\chi > 0$, ferromagnetic order) or counter-rotation ($\chi < 0$, antiferromagnetic order) among neighbouring walkers.

To quantify the relationship between the emergent collective behaviour and the pairwise orbital phase synchronization of adjacent walkers, we compute separately the mean phase difference $\Delta\phi_{\pm} \in [0, \pi]$ for co-rotating (+) and counter-rotating (−) walkers as

$$\Delta\phi_{\pm}(t) = \frac{1}{N_{p_{\pm}}} \sum_{i,j_{\pm}} |\phi_i(t) \mp \phi_j(t)|, \quad (5)$$

where ϕ_i is the instantaneous horizontal phase with respect to the lattice centreline (Fig. 1a), and $\sum_{i,j_{\pm}}$ denotes the sum over $N_{p_{\pm}}$ adjacent co-rotating (N_{p_+} and $i-j_+$) or counter-rotating (N_{p_-} and $i-j_-$) pairs of walkers. The phase difference thus allows us to identify if there is preference for in-phase ($\Delta\phi \rightarrow 0$) or out-of-phase ($\Delta\phi \rightarrow \pi$) rotation among adjacent walkers. We note that incoherent orbital synchronization corresponds to $\Delta\phi \rightarrow \pi/2$.

Data-acquisition protocol. To guarantee robust statistics, we develop a systematic data-acquisition protocol. The goal is to repeat multiple times a sufficiently long experiment to ensure that (i) the initial spin distribution is random, and (ii) the spin system reaches a statistically steady state. To guarantee random initial conditions, we manually stirred with a needle all the drops at the beginning of each run. By checking that the spin correlation started from 0 at the beginning of each experimental run, we confirmed that our stirring procedure was adequate. We also checked that the stirring did not disrupt the vertical synchronization of the walkers.

To determine the minimum time required for each experimental run, we performed preliminary tests to estimate the characteristic

autocorrelation time τ_i for the spin arrangement, which is computed through the autocorrelation function,

$$R(t) = \mathbf{S}(t=0) \cdot \mathbf{S}(t)/N, \quad (6)$$

as the first time for which $R(\tau_i) = 0$. Here, $\mathbf{S}(t)$ denotes the vector, with components $S_i(t)$, that characterizes the lattice spin arrangement at time t . The autocorrelation time provides a measure of the characteristic time beyond which the collective order at $t + \tau_i$ is statistically independent of the collective order at time t . Since τ_i fluctuates depending on the experimental realization, we define the length of the 'statistically independent interval' as

$$\tau_i = \langle \tau_i \rangle + \sigma(\tau_i), \quad (7)$$

where $\langle \tau_i \rangle$ and $\sigma(\tau_i)$ denote, respectively, the average and standard deviation resulting from 10 different realizations of a given lattice configuration. Our experiments show that τ_i is inversely related to the rate at which spins switch direction (higher switching rates lead to shorter τ_i), which in turn is a non-monotonic function of the forcing acceleration γ/γ_f . We thus recomputed τ_i as in equation (7) for each driving forcing in the range of interest (Fig. 1h). The largest $\tau_{i,\max} \approx 0.5$ h (lowest switching rate) was observed at $\gamma \approx \gamma_c$, the driving acceleration for which the signal-to-driving ratio for $S(t)$ is maximal (Fig. 1c), and the emergent collective behaviour strongest (Fig. 1h). Based on this observation, we selected 1 h (−1,800 circulations for each drop) as the recording length for our experimental realizations, thus guaranteeing that the system has more than enough time to reach a steady state. This typical run duration also yielded an optimal frequency to measure γ_f before and after each realization.

Following this protocol, we recorded as many 1-h videos as needed to obtain a minimum of $N_i \geq 8$ statistically independent intervals for each γ/γ_f level. In some cases the number of independent intervals was as high as $N_i \approx 50$. For each independent interval we then computed its associated spin–spin correlation $\chi_j(t)$. The data reported in Fig. 1h correspond to the resulting average, $\langle \sum \chi_j(t)/N_i \rangle$, and standard deviation, $\sigma(\sum \chi_j(t)/N_i)$, of these time series. The same data-acquisition protocol was followed for all lattices discussed in the main text, including those involving system rotation. We note that exceptions were made to obtain Figs. 1d, 2a, 3a, 4b, for which we conducted longer experiments to better illustrate the emergent collective phenomena.

Boundary conditions, ring curvature R , and lattice size N . Experiments were performed to determine the effects of the boundary conditions, lattice size N , and ring curvature R in 1D HSLs (Fig. 1a). To assess the effect of periodic versus non-periodic boundary conditions, we considered the antiferromagnetic configuration with $N = 20$ shown in the main text (Fig. 1), and repeated the experiment at $\gamma/\gamma_f = 86\%$ after plugging one of the submerged wells. We note that in the resulting non-periodic lattice with $N = 19$, the two end walkers were separated by a relatively large distance ($2L > 7\lambda_f$) by the thin layer ($H = 1$ mm) over which the waves dissipated quickly. Hence, the walkers at the ends did not interact with each other, as was checked by direct visualization of the wave field. Comparison of our experimental results revealed $\langle \chi(N=19) \rangle / \langle \chi(N=20) \rangle \approx 1.05$, which is well within the expected standard deviation, and so demonstrated a negligible effect of the boundary conditions. We also note that for 1D periodic lattices tuned for preferred antiferromagnetic order, it is important whether N is even or odd. An odd number of spins may lead to geometrical frustration effects⁹ that hinder the preferred collective order. To avoid such effects—the investigation of which is left for future studies—we selected even N for all experiments reported in the main text.

To assess the effect of lattice size, we compared experiments with $N = 10$ and $N = 20$, while keeping both L and R constant. Both sets of experiments led to preferred antiferromagnetic order, thus supporting

our inference that the emergent order is not a finite-size effect. We also compared these results with those of a 1D straight lattice ($R = \infty$) with $N=8$, where the same preferred order emerged. We may thus eliminate the curvature of the circular lattice from consideration as an important factor for the emergent collective behaviour. Finally, we also checked for finite-size effects in the 2D square lattices: experiments with $N=37$ and $N=49$ resulted in the same collective order.

Theory

Rayleigh–Bessel oscillator model. To rationalize the emergent order in HSLs, we extend the modelling framework for pilot-wave dynamics introduced previously⁶¹. In the weak-acceleration limit, $|\dot{\mathbf{v}}|T_M/|\mathbf{v}| \ll 1$, these authors show that the trajectory of a walking droplet, $\mathbf{x}(t)$, may be described by the equation

$$\frac{d}{dt}(m_w \mathbf{v}) + D_w \mathbf{v} = \mathbf{F}, \quad (8)$$

where $\mathbf{v} = \dot{\mathbf{x}}$ is the droplet velocity, \mathbf{F} an externally imposed force acting on the drop, $D_w(|\mathbf{v}|)$ the nonlinear drag, and m_w the effective walker mass. In the low-speed limit, in which the wave decay time, T_M , is much smaller than the time taken for the droplet to travel one Faraday wavelength, $T_M \ll \lambda_F/u_0$ (where u_0 is the free walking speed of a droplet), one may further simplify equation (8) to a Rayleigh oscillator-type equation⁶², similar to that introduced in a previous work⁶³, where the droplet trajectory is described by

$$m_w \frac{d\mathbf{v}}{dt} = D_R \left(1 - \frac{|\mathbf{v}|^2}{u_0^2}\right) \mathbf{v} + \mathbf{F}. \quad (9)$$

Here, D_R denotes the magnitude of the nonlinear Rayleigh-type drag, which drives the droplet towards its free walking speed, u_0 . The dependence of the model parameters m_w , u_0 and D_R on the physical variables is summarized in Extended Data Table 1. Equation (9) adequately describes the motion of weakly accelerating, relatively low-speed droplets. We note that both asymptotic limits are satisfied by orbiting droplets in the regime $\gamma \leq \gamma_c$, where $T_M \approx 0.1$ s. Although these limits are not strictly satisfied in the relatively short periods of time during which spin flips occur, our analysis will demonstrate that details of the spin flips are not essential to rationalize the emergent collective behaviour.

We consider N droplets self-propelling above an array of submerged circular wells with centre-to-centre separation L . Equation (9) determines the trajectory of each droplet, which is defined by a two-component displacement vector $\mathbf{x}_i(t)$, where $i = 1, \dots, N$. The force acting on each droplet may be decomposed into two components, $\mathbf{F} = \mathbf{F}_w + \mathbf{F}_{ij}$, where \mathbf{F}_w represents the effective confining force exerted by the submerged well, and \mathbf{F}_{ij} the wave force exerted on droplet i by its nearest neighbouring droplet j . Motivated by experiments⁶⁴, we assume that \mathbf{F}_w is a central force that points towards the well's centre.

As described in the main text, in the relatively low-memory regime ($\gamma \leq \gamma_c$), the drops remain on circular trajectories, with a fixed orbital radius r . Focusing on finite 1D lattices for the sake of simplicity, we may thus express the droplet trajectory and velocity vectors as $\mathbf{x}_i(t) = (r \cos \phi_i(t) + (i-1)L, r \sin \phi_i(t)) = r \hat{\mathbf{r}}_i + (i-1)L \hat{\mathbf{x}}$, and $\dot{\mathbf{x}}_i(t) = r \dot{\phi}_i(-\sin \phi_i(t), \cos \phi_i(t)) = r \dot{\phi}_i \hat{\boldsymbol{\theta}}_i$, respectively. Here, $\hat{\mathbf{r}}_i$ and $\hat{\boldsymbol{\theta}}_i$ denote the radial and azimuthal unit vectors for the i th spin with respect to the centre of its well, and $\hat{\mathbf{x}}$ the unit vector along the lattice centre line (Fig. 2e). Writing $\omega_i = \dot{\phi}_i$ and substituting $\mathbf{x}_i(t)$ and $\dot{\mathbf{x}}_i(t)$ into equation (9) yields the following equations for the normal and tangential force balances:

$$-m_w r \omega_i^2 = \mathbf{F} \cdot \hat{\mathbf{r}}_i, \quad (10)$$

$$m_w r \frac{d\omega_i}{dt} - D_R \left(1 - \frac{r^2 \omega_i^2}{u_0^2}\right) r \omega_i = \mathbf{F}_{ij} \cdot \hat{\boldsymbol{\theta}}_i. \quad (11)$$

We note that \mathbf{F}_w only appears in the radial force balance, where it acts to select the orbital radius r . Since the experiments suggest that emergent order in HSLs is driven primarily by synchronization of the droplets' relative orbital phase (Figs. 1f, 2c), we restrict our attention to the azimuthal force balance (equation (11)) and simply infer the value of r from our experiments. Thus, to rationalize the preferred mean phase differences, $\Delta\phi_s$, in terms of the droplet coupling force, \mathbf{F}_{ij} , we may write equation (11) as a nonlinear differential equation for the evolution of each droplet's angular frequency, $\omega_i(t)$,

$$\dot{\omega}_i = \frac{1}{\tau} \left(1 - \frac{\omega_i^2}{\omega_0^2}\right) \omega_i + \frac{\mathbf{F}_{ij} \cdot \hat{\boldsymbol{\theta}}_i}{m_w r}, \quad (12)$$

where $\omega_0 = u_0/r$ is the preferred angular frequency for a given driving acceleration γ , as would arise for a single drop orbiting in isolation, and $\tau = m_w/D_R$ is the relaxation timescale (see Extended Data Table 1).

To complete our spin model, we must define the wave-mediated force exerted by droplet j on droplet i , \mathbf{F}_{ij} . The stroboscopic model of ref.⁴² predicts that the wave field generated by the j th walker may be approximated by

$$\eta_j(\mathbf{x}, t) = \frac{A}{T_F} \int_{-\infty}^t J_0(k_F |\mathbf{x} - \mathbf{x}_j(s)|) e^{-(t-s)/T_M} ds, \quad (13)$$

where A , T_F and T_M are defined in Extended Data Table 1. Thus, the coupling force may be expressed as

$$\mathbf{F}_{i,j} = \frac{F}{T_F} \int_{-\infty}^t \frac{J_1(k_F |\mathbf{x}_i(t) - \mathbf{x}_j(s)|)}{|\mathbf{x}_i(t) - \mathbf{x}_j(s)|} (\mathbf{x}_i(t) - \mathbf{x}_j(s)) e^{-(t-s)/T_M} ds. \quad (14)$$

This expression was derived for droplets unperturbed by topography and so does not incorporate the additional wave damping expected in the shallow inter-well regions⁶⁵. Nevertheless, our visualization of the wave field produced by a single droplet in the lattice yielded a waveform notably similar in form to that expected on the basis of equation (14) (Methods section 'Wave coupling'). We also note that there is a relatively fast-propagating wavefront generated at impact³⁵, which decays rapidly with distance and so has a negligible influence on droplet pair interactions when the drops are separated by more than approximately λ_F (refs. 66,67). Guided by previous studies and experimental evidence, we thus neglect this capillary wavefront and consider that the liquid layer between wells has a negligible influence of the form of the drops' wave fields and so seek a simplification of equation (14) that yields insight into the mechanism responsible for the emergent order.

In the parameter regime of interest, $\gamma \leq \gamma_c$, the wave memory time, $T_M < 0.1$ s, is much smaller than the orbital period, $2\pi/\omega_0 \approx 2$ s. We may thus simplify equation (14) in the limit of $T_M \ll 2\pi/\omega_0$ to obtain

$$\mathbf{F}_{i,j} \approx \frac{FT_M}{T_F} J_1(k_F |\mathbf{x}_i(t) - \mathbf{x}_j(t)|) \frac{(\mathbf{x}_i(t) - \mathbf{x}_j(t))}{|\mathbf{x}_i(t) - \mathbf{x}_j(t)|}. \quad (15)$$

Substituting equation (15) into equation (12) yields a system of ODEs for each droplet interacting with its nearest neighbours in a spin lattice

$$\dot{\omega}_i = \frac{1}{\tau} \left(1 - \frac{\omega_i^2}{\omega_0^2}\right) \omega_i + \mathcal{F} \sum_j \left[J_1(k_F |\mathbf{x}_i - \mathbf{x}_j|) \frac{(\mathbf{x}_i - \mathbf{x}_j)}{|\mathbf{x}_i - \mathbf{x}_j|} \cdot (-\sin \phi_i, \cos \phi_i) \right]. \quad (16)$$

Here, \mathcal{F} is the interaction force coefficient, and \sum_j denotes the sum over nearest neighbours $j = i \pm 1$. Owing to the form of the coupling force, we refer to this as the 'Bessel model', which predicts the emergent spin order and phase synchronization in terms of three parameters (τ , ω_0 , \mathcal{F}) that may be deduced from the system's fluid properties, in addition to the lattice spacing, L , and the Faraday wavenumber, k_F . Expressions for the parameters τ , ω_0 and \mathcal{F} are provided in Extended

Article

Data Table 1, and their dependence on γ/γ_F is presented in Supplementary Fig. 1. Finally, we note that investigating precisely the collective order emerging from excited spin states, such as trefoils arising for $\gamma > \gamma_c$ (Fig. 1c), would require more involved models such as a full implementation of the stroboscopic model⁴², or the variable-topography model of a previous work⁶⁸.

Generalized Kuramoto model. By making a series of further approximations to the form of the coupling in the Bessel model (equation (16)), we now demonstrate that the emergent collective order in HSLs is governed by a generalization of the classical Kuramoto model for coupled phase oscillators⁴. From equation (16), the force on droplet i due to the adjacent droplet ($i+1$) is

$$\mathbf{F}_{i,i+1} = -\mathcal{F}J'_0(k_F|\mathbf{x}_i(t) - \mathbf{x}_{i+1}(t)|) \frac{(\mathbf{x}_i(t) - \mathbf{x}_{i+1}(t))}{|\mathbf{x}_i(t) - \mathbf{x}_{i+1}(t)|}. \quad (17)$$

We first make the approximation that the orbital radius is small relative to the centre-to-centre lattice separation, $r/L \ll 1$. This approximation is well satisfied in the experiments, where $r \leq 3$ mm and $L > 14$ mm, so $r/L \leq 0.2$. We can thus approximate the distance between the two droplets as $|\mathbf{x}_i(\phi_i) - \mathbf{x}_{i+1}(\phi_{i+1})| \approx L + r(\cos\phi_{i+1} - \cos\phi_i)$, and expand the azimuthal component of the wave-induced force:

$$\hat{\theta}_i \cdot \mathbf{F}_{i,i+1} \approx -\mathcal{F}[\sin\phi_i + (r/L)(\sin\phi_i - \sin\phi_{i+1})\cos\phi_i] J'_0(k_F L - k_F r(\cos\phi_i - \cos\phi_{i+1})). \quad (18)$$

We then make the additional approximation that

$$k_F r |(\cos\phi_i - \cos\phi_{i+1})| = 2k_F r \left| \sin\left(\frac{\phi_i - \phi_{i+1}}{2}\right) \sin\left(\frac{\phi_i + \phi_{i+1}}{2}\right) \right| \ll 1 \quad (19)$$

which may be written equivalently as

$$x_i - x_{i+1} \ll \frac{\lambda_F}{2\pi}, \quad (20)$$

where (x_i, y_i) are the Cartesian coordinates for each drop relative to the well centre. Although this limit will not be satisfied by all solutions of equation (16), for the range of L considered in our experimental study, the droplets exhibit in-phase synchronization ($\Delta\phi_i \approx 0$; Figs. 1f, 2c); consequently, the observed dynamics are expected to satisfy the approximation in equation (19).

Exploiting equation (19), we thus deduce that

$$J'_0(k_F L - k_F r(\cos\phi_i - \cos\phi_{i+1})) \approx J'_0(k_F L) - k_F r J''_0(k_F L)(\cos\phi_i - \cos\phi_{i+1}), \quad (21)$$

from which equation (18) indicates that

$$\hat{\theta}_i \cdot \mathbf{F}_{i,i+1} \approx -\mathcal{F}J'_0(k_F L)\sin\phi_i + \mathcal{F}k_F r J''_0(k_F L)(\cos\phi_i - \cos\phi_{i+1})\sin\phi_i - \frac{\mathcal{F}r}{L} J'_0(k_F L)(\sin\phi_i - \sin\phi_{i+1})\cos\phi_i. \quad (22)$$

Noting that the first term in equation (22) is cancelled when we sum the contribution of the forces from the two neighbouring droplets, $i-1$ and $i+1$, we may now express the coupling force as the gradient of a potential U , yielding a reduced model for the spin lattice system as

$$\dot{\omega}_i = \frac{1}{\tau} \left(1 - \frac{\omega_i^2}{\omega_0^2} \right) \omega_i - \sum_j \frac{\partial U_{i,j}}{\partial \phi_i}, \quad (23)$$

where the sum is only over nearest neighbours within the lattice. The generalized Kuramoto coupling potential, $U_{i,j}$, may be expressed as

$$U_{i,j} := U(\phi_i, \phi_j) = \frac{\alpha}{2} |\cos\phi_i - \cos\phi_j|^2 + \frac{\beta}{2} |\sin\phi_i - \sin\phi_j|^2 = \frac{\alpha}{2r^2} |x_i - x_j|^2 + \frac{\beta}{2r^2} |y_i - y_j|^2, \quad (24)$$

where

$$\alpha = \mathcal{F}k_F r J''_0(k_F L), \quad (25)$$

$$\beta = (\mathcal{F}r/L)J'_0(k_F L). \quad (26)$$

We refer to this system as the ‘generalized Kuramoto’ (GK) model, and illustrate the dependence of the ratio β/α on lattice spacing, L , in Supplementary Fig. 2. We note that the form of the potential U is prescribed only by the local wave curvature and gradient, through the signs and relative magnitudes of α and β . Consequently, the amplitude of the local wave field does not substantially alter the form of the potential, U , which further justifies the neglect of topography-induced wave damping. We note that our GK model (equation (23)) includes inertia, as do the Kuramoto-like models typically used to study synchronization phenomena in power grids^{69,70}.

Notably, we found that the GK model succeeds in rationalizing the emergent order even at intermediate values of lattice spacing, L , for which the approximation equation (19) is not necessarily satisfied. To understand this unforeseen success of the GK model, we compare the form of the Bessel coupling force (equation (16)) with that expected from the GK model (equation (23)) for all ϕ_i and ϕ_j and four representative lattice separations (Supplementary Fig. 3). In all four cases, we find that the GK coupling corresponds to the two fundamental Fourier modes of the Bessel coupling, which explains the agreement between the predictions of the Bessel and GK models over the range of lattice spacings of interest. For smaller values of L , we find that the agreement holds until the spacing becomes comparable to the orbital radius, $L \approx 2r$. In the limit of $rk_F \ll 1$, when the orbital radius is much smaller than the Faraday wavelength, the approximation (equation (19)) is strictly satisfied. Finally, we note that the amplitude of the GK coupling force computed via the predictions (equations (25), (26)) is a factor of two larger than the amplitude of the dominant Fourier modes computed from the Bessel force (Supplementary Fig. 3). As discussed in Extended Data Fig. 5, we compensate for this overestimation in order to obtain the quantitative agreement between the experiments and the GK model (equation (23)).

Spin flips and wave coupling. Our theory indicates that, in the parameter regime considered in our experimental study, the fundamental mechanism responsible for the emergent collective order does not depend strongly on either the precise details of the spin flips or the small deformation of the walker wave field due to variations in bottom topography. Nevertheless, we detail these effects here for the sake of completeness.

Spin flips. Extended Data Fig. 2 (Supplementary Video 6) illustrates a typical spin flip event as observed in our experiments with the 1D antiferromagnetic HSL described in Fig. 1. Owing to transient rearrangements from the random initial conditions, at some time t during this experimental run, three neighbouring spins happen to be rotating in the same direction (see Extended Data Fig. 2a). Since the lattice geometry promotes antiferromagnetic order, this local arrangement is not a preferred state. The collective interactions are such that the trajectory of the middle walker then starts to become elliptical (see Extended Data Fig. 2b). The elongation of the ellipse continues until the walker executes quasi-rectilinear motion across the well centre (see Extended Data Fig. 2c). Subsequently, the process is reversed, the result being the walker rotating in the opposite direction (see Extended Data Fig. 2d). After the spin flip, which typically takes 5 ± 1 s, the three walkers rotate in the preferred antiferromagnetic configuration (see Extended Data

Fig. 2e). When the collective order is strongest ($\gamma/\gamma_F \approx 86\%$ in Fig. 1h), the duration of a flip, of the order of 5 s, is negligible relative to the characteristic flipping period, of the order of 5–10 min. At higher accelerations, when the walkers switch direction much more frequently and the coherent order is lost ($\gamma/\gamma_F > 90\%$ in Fig. 1h), the duration of the flips becomes comparable to the flipping period. We note that ferromagnetic lattices, such as those shown in Fig. 2, undergo similar spin flips.

Wave coupling. A rough estimate of the extent to which the variable bottom topography will alter the form of the wave field relative to that predicted by the stroboscopic model (equation (13)) may be obtained by comparing the Faraday wavelengths given by the water-wave dispersion relation for the shallow λ_F^H and deep λ_F^h regions. As noted earlier in the experimental description, these wavelengths are only marginally different for our choice of parameters, specifically $\lambda_F^h/\lambda_F^H \approx 1.05$. One thus expects that the walker wave field in our lattices will not be appreciably different from that previously predicted⁴². Indeed, as shown in Extended Data Fig. 3a, b, direct visualization of waves generated by a single walker reveals a wave form comparable to that expected from a superposition of sub-harmonic zeroth-order Bessel functions, as in equation (13). We note that over the range of parameters considered in our study, no exotic Faraday patterns were excited, such as those arising in nonlinear regimes^{71,72} or excited by droplets walking in elliptical corrals⁴⁸.

To provide a quantitative characterization of the wave coupling, including the spatial decay³⁶, we perform additional simulations with a previously developed model⁶⁸, wherein changes in topography are incorporated through their influence on the local wave speed. We note that this model solves the wave problem explicitly, and has been benchmarked against experiments in a number of settings involving walkers interacting with submerged topography^{37,73–75}. In accordance with our experimental observations, we find that the simulated wave field has a form similar to that of a J_0 Bessel function (see Extended Data Fig. 3c). By taking into consideration spatial damping, it has been demonstrated³⁶ that in the deep-fluid regime, the wave field generated by a bouncing drop located at \mathbf{x}_j may be approximated by

$$h(|\mathbf{x} - \mathbf{x}_j|) = 2A\sqrt{b}J_0(k_F|\mathbf{x} - \mathbf{x}_j|)|\mathbf{x} - \mathbf{x}_j|K_1(2\sqrt{b}|\mathbf{x} - \mathbf{x}_j|) \quad (27)$$

where K_1 is the modified Bessel function of the second kind. Our simulations indicate that the fitting parameters are $A \approx 15.4 \mu\text{m}$ and $b \approx 0.002 \text{ mm}^{-2}$, which is roughly consistent with previous free-surface synthetic Schlieren experiments⁷⁶. We note that the spatial damping included in equation (27) does not play a crucial role in rationalizing the mechanism responsible for the emergent collective order; thus, we can safely neglect its effects. Finally, we note that experiments support our assumption that the nearest-neighbour couplings are dominant: the waves become negligible before reaching the second-nearest wells.

Comparison to experiment. We proceed by comparing the results of our experimental study with the theoretical predictions of both the full wave coupling Bessel model (equation (16)), and the generalized Kuramoto model (equation (23)). Specifically, we characterize the dependence of the collective lattice order on both the well separation, L , and vibrational acceleration, γ , and demonstrate that the emergent orbital phase synchronization is determined by the form of the coupling force.

We compare the predictions of our theoretical models to the experimental results through the average spin-correlation, $\langle \chi \rangle$. In the simulations, for every data point, we perform N_t independent trials of a given lattice. We initialize each simulation with random initial conditions (ϕ_0, ω_0) for each droplet, independently drawn from uniform distributions with $\phi_0 \in [0, 2\pi]$ and $\omega_0 \in [-3\omega_0/2, 3\omega_0/2]$ to ensure a large spread. From each independent simulation, we compute a spin correlation time series $\chi_n(t)$, for $n = 1, \dots, N_t$, as defined in equation (4). We then compute the average of the instantaneous spin correlations across all trials as

$$\chi(t) = \frac{1}{N_t} \sum_{n=1}^{N_t} \chi_n(t). \quad (28)$$

We compute the final average spin correlation, $\langle \chi \rangle$, by time-averaging over the final quarter of this time series, so as to eliminate any influence of the initial transient regime. In our simulations of equations (16) and (23), this transient period is generally < 100 s. To guarantee robust statistics, we perform all simulations up to a time $t_{\text{max}} \approx 300\text{--}600$ s. We note that, owing to the approximations made in our modelling of the wave form, the preferred collective order is attained more rapidly in simulations than experiments.

We perform numerical tests to ensure that our results are not affected by either an insufficient number of trials or finite-size effects. Our simulations indicate that the collective behaviour becomes largely independent of the number of trials for $N_t = 200$ (Supplementary Fig. 4a). Similarly, our exploration of the effect of lattice size on the spin correlation (Supplementary Fig. 4b) reveals that the statistics become independent of the number of spins for $N \approx 150$. We thus select $N_t = 200$ and $N = 150$ for all subsequent simulations.

Varying lattice spacing. As demonstrated experimentally (Fig. 2), there exists a transition from antiferromagnetic to ferromagnetic order when the well separation, L , decreases from 17.7 to 13.2 mm. Continuously varying L is extremely prohibitive experimentally; thus, we proceed to do so using simulations.

We computed the average spin correlation, $\langle \chi \rangle$, in terms of the lattice spacing, L , via the Bessel model (equation (16)). For our simulations, we select a relaxation time of $\tau = 0.4$ s, an angular velocity of $\omega_0 = 3.3 \text{ s}^{-1}$, and an interaction coefficient of $\mathcal{F} = 70 \text{ s}^{-2}$, values consistent with the experimental range $\gamma \leq \gamma_c$ (Supplementary Fig. 1). We prescribe the orbital radius to be $r = 1.2$ mm, which is close to the average observed experimentally with $L = 13.2$ mm. The Faraday wavelength in the simulation is fixed at $\lambda_F = 2\pi/k_F = 4.95$ mm. We vary the well-to-well separation L across one Faraday wavelength, between 13 and 18 mm.

We present the dependence of the time-averaged spin correlation, $\langle \chi \rangle$, on lattice spacing, L , in Extended Data Fig. 4a. Our results show that the preferred collective behaviour oscillates between regions of positive and negative spin correlation as the lattice separation is varied. To better characterize the emergent ferromagnetic and antiferromagnetic order, we also compute the mean droplet phase difference, $\langle \Delta\phi_{\pm} \rangle$ (see Extended Data Fig. 4b), which reveals that the collective lattice behaviour is dominated by not two but four synchronization modes (see Extended Data Fig. 4c, d).

In the first ferromagnetic region, denoted FM_+ , the model predicts that $\langle \Delta\phi_{\pm} \rangle \approx 0$, indicating that neighbouring pairs of spins are on average in phase in the azimuthal direction, regardless of whether they co-rotate or counter-rotate. The bias towards ferromagnetic order (see Extended Data Fig. 4a) is thus associated with the dominance of the co-rotating synchronization mode over the counter-rotating mode (see Extended Data Fig. 4c, d). Similarly, in the antiferromagnetic region denoted by AFM_+ , we again observe a vanishing mean phase difference, $\langle \Delta\phi_{\pm} \rangle \approx 0$, indicating in-phase orbital motion, but now the relative dominance of the two synchronization modes is reversed. By contrast, the ferromagnetic and antiferromagnetic regions denoted by FM_- and AFM_- , respectively, result from two different synchronization modes that are characterized by out-of-phase orbital motion, $\langle \Delta\phi_{\pm} \rangle \approx \pi$ (see Extended Data Fig. 4c, d). The relative dominance of these modes thus determines the bias towards positive or negative spin correlation (see Extended Data Fig. 4a).

The origins of these four forms of collective order are rationalized through the generalized Kuramoto model (equation (23)). By examining the dependence of the control parameters α and β , as defined in equations (25), (26), on lattice spacing L , we note that the four dynamical modes are those that precisely minimize the reduced coupling potential U (equation (24)). Specifically, when $\alpha > 0$, which happens when $J_0''(k_F L) > 0$, corresponding to FM_+ (see Extended Data Fig. 4a),

Article

the first term of the coupling potential U strongly favours motion for which $|x_i - x_j|$ is minimized. In-phase rotation is thus preferred, but this condition is equally satisfied by both co- and counter-rotating spins (see Extended Data Fig. 4c, d, column A). The observed bias towards ferromagnetic order thus comes from the minimization of the second term in U , which is determined by the sign of β , and so by the local slope $J'_0(k_F L)$. In particular, $\beta > 0$ in the FM₊ region (see Extended Data Fig. 4a), indicating that, between the two possible in-phase modes, the system will favour the co-rotating mode because it also minimizes $|y_i - y_j|$ (see Extended Data Fig. 4c, d). The emergence of ferromagnetic order FM₊ is thus rationalized. Similar arguments may provide rationale for the observed order in the remaining regions. For instance, as arises for FM₋, $\alpha > 0$ in AFM₊ and so in-phase rotation is preferred. However, since $\beta < 0$, the system promotes counter-rotating spins as those now minimize the potential U by maximizing $|y_i - y_j|$. We note the regions where no preferred collective order emerges (see Extended Data Fig. 4a) precisely correspond to the extrema and inflection points of $J_0(k_F L)$, at which either $\alpha = 0$ or $\beta = 0$. Finally, we note that simulations of the Bessel model (equation (16)) with 50×50 lattices confirmed that a similar dependence of collective order on lattice spacing emerges for substantially larger 2D square lattices (see Extended Data Fig. 6a).

Varying interaction strength. In Extended Data Fig. 5, we compare the experimentally observed dependence of the average spin correlation, $\langle \chi \rangle$, on the bath acceleration, γ/γ_F , with the predictions based on both the Bessel model (equation (16)) and the generalized Kuramoto model (equation (23)). For values of γ/γ_F just beyond the walking threshold, both models predict the relatively weak spin correlations associated with relatively weak coupling. As the coupling strength is increased progressively, both models predict the emergence of a more pronounced antiferromagnetic response, up to a critical acceleration γ_c , where $\min(\chi) \approx -0.4$, in excellent agreement with the experiments. Beyond this optimal driving, the magnitude of the spin correlation decays rapidly, until the preferred collective order vanishes. Strictly speaking, the validity of our theoretical models is restricted to $\gamma \leq \gamma_c$, where the droplet motion is confined to circular orbits. Nevertheless, both models capture the decay of the antiferromagnetic order beyond γ_c . Experimentally, such decay is related to the destabilization of circular orbits into trefoil-like trajectories (Fig. 1h) that in turn prompts chaotic switching in orbital direction. In both theoretical models, similar chaotic switching emerges as the coupling parameters, \mathcal{F} and α, β , are increased to values corresponding to $\gamma > \gamma_c$. Similar simulations with both the Bessel (equation (16)) and generalized Kuramoto (equation (23)) models were conducted for a 50×50 lattice in order to confirm that the same collective order emerges in 2D square lattices for variable memory (see Extended Data Fig. 6d).

Bath rotation. We conclude by generalizing our theoretical framework to rationalize the transition from antiferromagnetic to ferromagnetic order induced by applying a constant rotation, Ω , to the vibrating bath (Fig. 3a–e).

We recall that the rotating bath surface is an equipotential; consequently the radially outward centrifugal force on the drop is precisely balanced by the inward interfacial force resulting from the parabolic bath surface and so need not be considered henceforth⁸. The effect of bath rotation may thus be incorporated into our modelling through the addition of the Coriolis force, $\mathbf{F}_c = -2m\boldsymbol{\Omega} \times \mathbf{x}$ (ref. ⁴⁷), which acts in the inward radial direction for circular cyclonic/anticyclonic orbits. To correctly model the HLS dynamics in a rotating frame, we should thus include the radial force balance into our models. To proceed, we model the force exerted by the well in the low-memory regime by a confining radial potential of the form $V(r) = kr^4$, so that $\mathbf{F}_w = -dV/d\mathbf{r}$, where $r = |\mathbf{x}|$ (ref. ⁶⁴). We find that the fourth-order degree of the potential captures adequately the abrupt influence of topography at the well boundary. We select the strength of the potential, k , so that the predictions for the free walking speed u_0 and experimentally observed orbital

radius r are consistent with our experimental observations in the absence of rotation (Fig. 1c).

Focusing on the wave-mediated droplet coupling \mathbf{F}_{ij} as approximated by the generalized Kuramoto force (equation (23)), we may thus write the 2D version of the Rayleigh oscillator equation (9), with an applied force $\mathbf{F} = \mathbf{F}_c + \mathbf{F}_w + \mathbf{F}_{ij}$ as

$$\ddot{\mathbf{x}}_i = \frac{1}{\tau} \left(1 - \frac{|\dot{\mathbf{x}}_i|^2}{u_0^2} \right) \dot{\mathbf{x}}_i - 4k|\mathbf{x}_i|^2 \mathbf{x}_i - 2\boldsymbol{\Omega} \times \dot{\mathbf{x}}_i + \sum_j \mathbf{F}_{i,j}(\mathbf{x}_i, \mathbf{x}_j, L). \quad (29)$$

Noting that the orbital radius is now a variable $r_i(t)$, we may express the droplet position around the centre of the i th well in polar coordinates as

$$\mathbf{x}_i(t) = r_i(t)(\cos \phi_i(t), \sin \phi_i(t)). \quad (30)$$

Since full resolution of the droplet's dynamics in the presence of rotation is beyond the scope of the theory presented here, we simplify the equations to rationalize the observed behaviour. We thus neglect the contribution of \dot{r}_i to the Rayleigh drag term, which is valid provided that $\dot{r}_i^2 \ll r_i^2 \omega_i^2$, and the contribution of the Rayleigh drag term in the radial equation, which is valid provided that $|\dot{r}_i| \ll \tau r_i \omega_i^2$. Since the droplet–droplet interaction primarily drives the phase synchronization between the droplets, we also neglect the wave-mediated interaction force from the radial force balance. Finally, we assume that the interaction force does not vary with the orbital radius, so that α and β are held constant, which is valid provided the droplet trajectories do not deviate substantially from circles. With these assumptions, we may then substitute equation (30) into equation (29) to yield

$$\ddot{r}_i = r_i \omega_i^2 + 2\Omega \omega_i r_i - 4kr_i^3, \quad (31)$$

$$\dot{\omega}_i = \frac{1}{\tau} \left(1 - \frac{r_i^2 \omega_i^2}{u_0^2} \right) \omega_i - \frac{2\dot{r}_i}{r_i} (\Omega + \omega_i) - \sum_j \frac{\partial U_{i,j}}{\partial \phi_i}. \quad (32)$$

The numerical prediction of the model formed by equations (31) and (32) are compared with our experimental results in Fig. 3e, showing excellent agreement given the level of theory reduction. Simulations are performed with $N = 150$ spins and $N_t = 200$ independent trials. We fix $\tau = 0.1$ s, $u_0 = 6$ mm s⁻¹, $r = 1.8$ mm, $k = 4.34$ mm⁻² s⁻², $\alpha = 10$ s⁻² and $\beta = -1.5$ s⁻². We then vary the rotation rate, Ω , over the range $0 < \Omega < 0.7$ s⁻¹ as in the experiments. Our results reveal a dependence of the average spin correlation, $\langle \chi \rangle$, on the rotation rate, Ω , very similar to that observed in the laboratory.

Tunability

HSLs also offer the opportunity to investigate more exotic forms of collective behaviour and frustration effects induced by wave-mediated interactions. Here, we provide several proof-of-concept experiments and simulations in order to illustrate their potential for future research.

As discussed in Methods section ‘Stationary bath’, it is possible to deduce the vertical phase of the droplets by observing the light reflected from the upper side of the droplets, which intensifies when the droplets deform during impact. Since the walkers bounce sub-harmonically with respect to the bath vibration, drops may bounce vertically in-phase or out-of-phase with respect to their neighbours (see Extended Data Fig. 7a). Vertically out-of-phase walkers are coupled through a wave field equal to that of in-phase walkers but with the opposite sign (see Extended Data Fig. 4). Consequently, for example, the emergent order of an HSL, whose lattice spacing promotes orbital in-phase antiferromagnetic order AFM₊ for vertically in-phase walkers, will shift to out-of-phase antiferromagnetic order AFM₋ for vertically out-of-phase walkers (see Extended Data Fig. 7a). An HSL with walkers with random vertical phases will thus produce an antiferromagnetic

state with competing orbital synchronization that effects the emergent spin correlation (see Extended Data Fig. 7b). Other forms of frustration can be investigated by changing the lattice geometry in 2D. For example, a triangular lattice (see Extended Data Fig. 7c) in which the spacing is tuned to promote antiferromagnetic order leads to degenerate ground states, the investigation of which is expected to yield insights into how wave-coupled spin lattices respond to geometric frustration⁷⁷.

We also perform simulations using a previously published model⁶⁸ that solves the wave field explicitly, in order to demonstrate how alterations of the basic experimental setup might allow one to tailor the coupling between spins and so study more exotic collective phenomena. We note that in these simulations, all the walkers are bouncing vertically in phase. We first confirm that orbital in-phase ferromagnetic FM₊ and antiferromagnetic AFM₊ orders are reproduced with the model⁶⁸ (see Extended Data Fig. 8). We proceed by simulating a lattice where the horizontal spacing promotes FM₊, while the vertical spacing promotes AFM₊ (see Extended Data Fig. 9a, left). Drops along the horizontal lines are thus rotating in phase, but their direction alternates vertically in an antiferromagnetic fashion (see Extended Data Fig. 9a, centre and right).

Next, we take as reference the ferromagnetic HSL (see Extended Data Fig. 8a) and repeat the simulation with a lattice where the centre of each well has been shifted by a random distance $\pm\epsilon$ in the horizontal and vertical directions (see Extended Data Fig. 9b, left). As the degree of randomness increases, the walkers' trajectories become less regular; thus, it becomes more difficult for the walkers to maintain precise in-phase orbital motion (see Extended Data Fig. 9b, centre and right).

In our third demonstration, with the same FM₊ as the reference (see Extended Data Fig. 8a), we alternate the sizes of the bouncing droplets, thereby mixing two 'species of spins' with different frequency and inertia (see Extended Data Fig. 9c, left). Although the drop size does not change the preferred mode of synchronization, which is dictated by the lattice spacing, the different rotation frequencies lead to frustration. Notably, the drops adjust their orbital radii (see Extended Data Fig. 9c, centre) in order to match their rotation frequencies, as can be deduced from the equal slope of the $\phi(t)$ signals (see Extended Data Fig. 9c, right).

In our fourth demonstration, we reduce the local liquid depth along alternating columns of a FM₊ lattice geometry (see Extended Data Fig. 9d, left). As a result, the waves above the new submerged barriers dissipate waves more effectively (see Extended Data Fig. 9d, centre). Walkers are thus subjected to lateral couplings of different strengths, which leads to pairs whose phase is either strongly or weakly correlated (see Extended Data Fig. 9d, right), and so to the possibility of exploring SSH-type couplings as studied in topological insulators⁷⁸. We also note that the driving frequency can be used to dynamically tune the wavelength, range, and amplitude of the oscillatory coupling. Moreover, one might superimpose random fluctuations on the vibrational driving in order to study the effects of imposed white or coloured noise.

HSLs offer the opportunity to explore other potentially fruitful directions. One of them is the analysis of the collective order emerging from higher excited spin states such as trefoils and lemniscates⁴⁴, which emerge with larger well diameters⁶⁴, and at higher driving acceleration (Fig. 1c). Notably, the accompanying theoretical rationalization would require more involved models, such as a full implementation of the stroboscopic model⁴² or the variable-topography model⁶⁸. Similarly, the liquid depth, lattice geometry, and vibrational acceleration could be tuned to study the effects of longer-range oscillatory couplings beyond the nearest-neighbour interactions considered in this study, which might lead to more exotic dynamical states. HSLs thus offer the opportunity to investigate macroscopic dynamics analogous to those involving the oscillatory Ruderman–Kittel–Kasuya–Yosida (RKKY)³⁸ electronic spin coupling. Finally, investigating the similarities and differences between the collective synchronization arising in HSLs and other active systems might also prove fruitful. For example, it is known

that rotating vortices in reaction–diffusion systems may be coupled by nonlinear spiral waves^{79–82}.

Data availability

The data that support the findings of this study are available from the corresponding authors upon reasonable request.

41. Oza, A. U., Rosales, R. R. & Bush, J. W. M. Hydrodynamic spin states. *Chaos* **28**, 096106 (2018).
42. Oza, A. U., Rosales, R. R. & Bush, J. W. M. A trajectory equation for walking droplets: hydrodynamic pilot-wave theory. *J. Fluid Mech.* **737**, 552–570 (2013).
43. Labousse, M. et al. Self-attraction into spinning eigenstates of a mobile wave source by its emission backreaction. *Phys. Rev. E* **94**, 042224 (2016).
44. Perrard, S. et al. Self-organization into quantized eigenstates of a classical wave-driven particle. *Nat. Commun.* **5**, 3219 (2014).
45. Eddi, A. et al. Level splitting at macroscopic scale. *Phys. Rev. Lett.* **108**, 264503 (2012).
46. Harris, D. M. & Bush, J. W. M. Droplets walking in a rotating frame: from quantized orbits to multimodal statistics. *J. Fluid Mech.* **739**, 444–464 (2014).
47. Oza, A. U. et al. Pilot-wave dynamics in a rotating frame: on the emergence of orbital quantization. *J. Fluid Mech.* **744**, 404–429 (2014).
48. Sáenz, P. J., Cristea-Platon, T. & Bush, J. W. M. Statistical projection effects in a hydrodynamic pilot-wave system. *Nat. Phys.* **14**, 315–319 (2018).
49. Eddi, A. et al. Archimedean lattices in the bound states of wave interacting particles. *Europhys. Lett.* **87**, 56002 (2009).
50. Eddi, A., Boudaoud, A. & Couder, Y. Oscillating instability in bouncing droplet crystals. *Europhys. Lett.* **94**, 20004 (2011).
51. Thomson, S. J., Couchman, M. M. P. & Bush, J. W. M. Collective vibrations of confined levitating droplets. *Phys. Rev. Fluids* **5**, 083601 (2020).
52. Thomson, S. J., Durey, M. & Rosales, R. R. Collective vibrations of a hydrodynamic active lattice. *Proc. R. Soc. A* **476**, 20200155 (2020).
53. Couchman, M. M. P. & Bush, J. W. M. Free rings of bouncing droplets: stability and dynamics. *J. Fluid Mech.* **903**, A49 (2020).
54. Nachbin, A. Walking droplets correlated at a distance. *Chaos* **28**, 096110 (2018).
55. Nachbin, A. Kuramoto-like synchronization mediated through Faraday surface waves. *Fluids* **5**, 226 (2020).
56. Whitham, G. B. *Linear and Nonlinear Waves* (Wiley, 1974).
57. Douady, S. Experimental study of the Faraday instability. *J. Fluid Mech.* **221**, 383–409 (1990).
58. Harris, D. M. & Bush, J. W. M. Generating uniaxial vibration with an electrodynamic shaker and external air bearing. *J. Sound Vibrat.* **334**, 255–269 (2015).
59. Faraday, M. On a peculiar class of acoustical figures and on certain forms assumed by groups of particles upon vibrating elastic surfaces. *Philos. Trans. R. Soc. Lond.* **121**, 299–340 (1831).
60. Harris, D. M., Liu, T. & Bush, J. W. M. A low-cost, precise piezoelectric droplet-on-demand generator. *Exp. Fluids* **56**, 83 (2015).
61. Bush, J. W. M., Oza, A. U. & Moláček, J. The wave-induced added mass of walking droplets. *J. Fluid Mech.* **755**, R7 (2014).
62. Turton, S. E. *Theoretical Modeling of Pilot-wave Hydrodynamics*. PhD thesis, Massachusetts Institute of Technology (2020).
63. Labousse, M. & Perrard, S. Non-Hamiltonian features of a classical pilot-wave dynamics. *Phys. Rev. E* **90**, 022913 (2014).
64. Cristea-Platon, T., Sáenz, P. J. & Bush, J. W. M. Walking droplets in a circular corral: quantisation and chaos. *Chaos* **28**, 096116 (2018).
65. Tadriss, L. et al. Faraday instability and subthreshold Faraday waves: surface waves emitted by walkers. *J. Fluid Mech.* **848**, 906–945 (2018).
66. Galeano-Rios, C. A. et al. Ratcheting droplet pairs. *Chaos* **28**, 096112 (2018).
67. Couchman, M. M. P., Turton, S. E. & Bush, J. W. M. Bouncing phase variations in pilot-wave hydrodynamics and the stability of droplet pairs. *J. Fluid Mech.* **871**, 212–243 (2019).
68. Faria, L. M. A model for Faraday pilot waves over variable topography. *J. Fluid Mech.* **811**, 51–66 (2017).
69. Filatrella, G., Nielsen, A. H. & Pedersen, N. F. Analysis of a power grid using a Kuramoto-like model. *Eur. Phys. J. B* **61**, 485–491 (2008).
70. Rohden, M. et al. Self-organized synchronization in decentralized power grids. *Phys. Rev. Lett.* **109**, 064101 (2012).
71. Chen, P. & Wu, K.-A. Subcritical bifurcations and nonlinear balloons in Faraday waves. *Phys. Rev. Lett.* **85**, 3813–3816 (2000).
72. Périnet, N., Juric, D. & Tuckerman, L. S. Alternating hexagonal and striped patterns in Faraday surface waves. *Phys. Rev. Lett.* **109**, 164501 (2012).
73. Pucci, G. et al. Non-specular reflection of walking droplets. *J. Fluid Mech.* **804**, R3 (2016).
74. Pucci, G. et al. Walking droplets interacting with single and double slits. *J. Fluid Mech.* **835**, 1136–1156 (2018).
75. Harris, D. M. et al. The interaction of a walking droplet and a submerged pillar: from scattering to the logarithmic spiral. *Chaos* **28**, 096105 (2018).
76. Damiano, A. P. et al. Surface topography measurements of the bouncing droplet experiment. *Exp. Fluids* **57**, 163 (2016).
77. Diep, H. T. *Frustrated Spin Systems* (World Scientific, 2004).
78. Qi, X.-L. & Zhang, S.-C. Topological insulators and superconductors. *Rev. Mod. Phys.* **83**, 1057–1110 (2011).
79. Biktasheva, I. V. & Biktashev, V. N. Wave–particle duality of spiral waves dynamics. *Phys. Rev. E* **67**, 026221 (2003).
80. Biktasheva, I. V. et al. Computation of the drift velocity of spiral waves using response functions. *Phys. Rev. E* **81**, 066202 (2010).

Article

81. Azhand, A., Totz, J. F. & Engel, H. Three-dimensional autonomous pacemaker in the photosensitive Belousov–Zhabotinsky medium. *Europhys. Lett.* **108**, 10004 (2014).
82. Totz, J. F., Engel, H. & Steinbock, O. Spatial confinement causes lifetime enhancement and expansion of vortex rings with positive filament tension. *New J. Phys.* **17**, 093043 (2015).

Acknowledgements We gratefully acknowledge financial support from the NSF through CMMI-1727565 (J.W.M.B. and P.J.S.) and DMS-1719637 (R.R.R.), MIT Solomon Buchsbaum Research Fund (J.D.), and CNRS Momentum programme (G.P.).

Author contributions P.J.S. conceived the study, led the experimental developments and the writing of the paper, and contributed to the theoretical modelling. S.E.T. and R.R.R. contributed to the theoretical modelling. G.P. contributed to the conception and execution of the

preliminary experiments. A.G. contributed to the preliminary experiments. J.D. contributed to the theoretical modelling and the writing of the paper. J.W.M.B. contributed to the conception of the experiments and theory, and to writing the paper.

Competing interests The authors declare no competing interests.

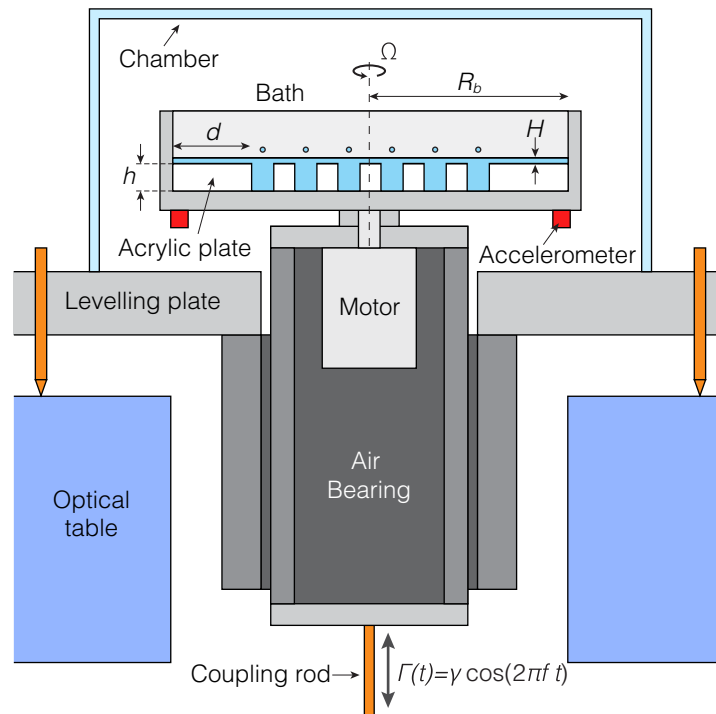
Additional information

Supplementary information The online version contains supplementary material available at <https://doi.org/10.1038/s41586-021-03682-1>.

Correspondence and requests for materials should be addressed to P.J.S. or J.W.M.B.

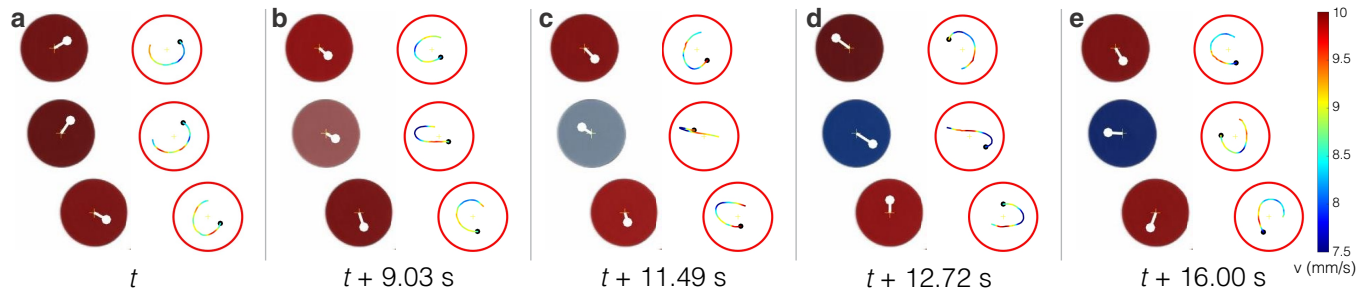
Peer review information *Nature* thanks Michael Shats and the other, anonymous, reviewer(s) for their contribution to the peer review of this work.

Reprints and permissions information is available at <http://www.nature.com/reprints>.



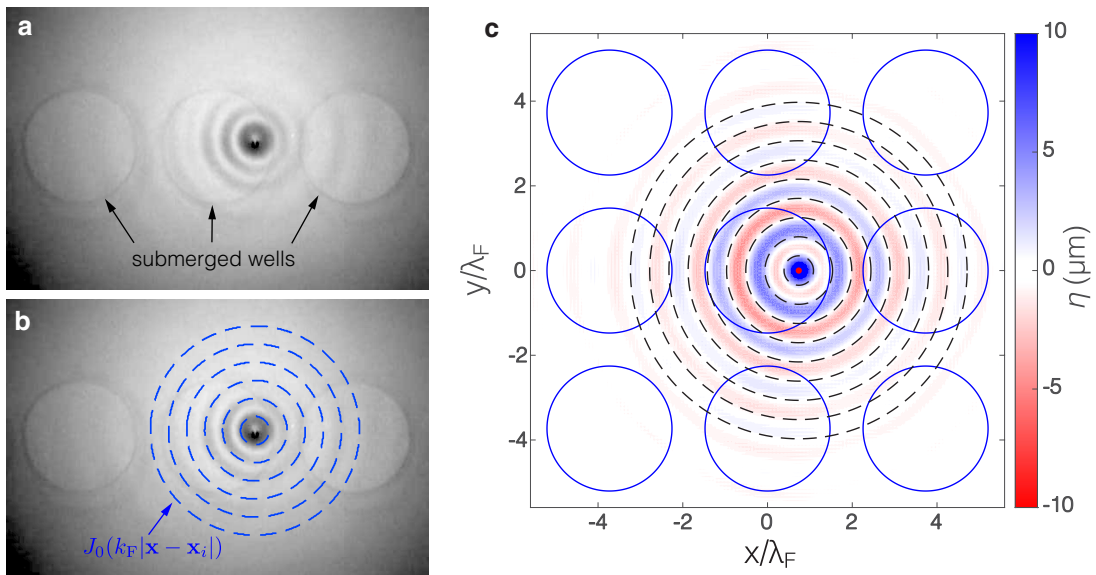
Extended Data Fig. 1 | Schematic of the experimental set-up. The test section was mounted on an optical table and vibrated vertically by an electromagnetic shaker. The shaker was connected to the bath by a thin steel rod coupled with a linear air bearing. The forcing acceleration was monitored

by two piezoelectric accelerometers. The bath was enclosed within a transparent acrylic chamber to ensure that ambient air currents did not affect the experiments. A d.c. motor housed inside the hollow air bearing enabled system rotation.



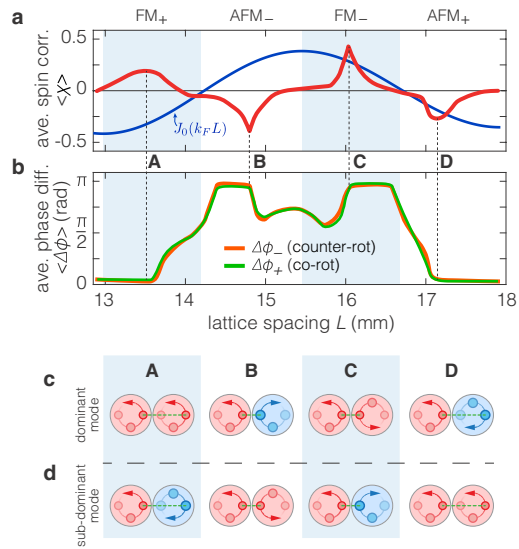
Extended Data Fig. 2 | Experimental spin flips. a–e. Snapshots at different times illustrate a typical spin-flip event arising in a 1D spin lattice (Supplementary Video 6). At each time, the panels at left are colour-coded according to the instantaneous spin S_i (same colour map as in Fig. 1d), while those on the right depict the recent walker trajectories, colour-coded according to the local speed. Perturbed by the wave fields emitted by its

neighbours, the middle walker initially follows an elliptical path. The length of the minor axis decreases until the walker trajectory essentially becomes a straight line across the well centre. Subsequently, the process is reversed, resulting in the walker rotating in the opposite sense. The three walkers shown are part of the 1D antiferromagnetic lattice described in Fig. 1h with $\gamma/\gamma_T = 86.0\%$.

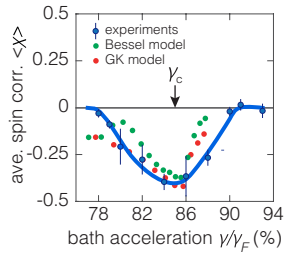


Extended Data Fig. 3 | Wave coupling. **a**, Experimental visualization of the wave field generated by a single walker in a 1D lattice with the same geometry as in Fig. 1h and $\gamma/\gamma_F = 92.0\%$. The submerged wells can be identified as the regions with a different shade of grey. **b**, Superposition of the wave field shown in **a** and the zeros of the drop-centred Bessel function $J_0(k_F|x-x_i|)$. **c**, Wave field of a

bouncer computed with the theoretical model developed previously⁶⁸ for walkers over variable topography. The bouncer is located at $(x,y) = (3D/8, 0)$ in a 2D square lattice with the same well diameter D and centre-to-centre separation L as in **a** and $\gamma/\gamma_F = 88.0\%$. Solid blue lines denote the submerged wells and dashed lines the zeros of a Bessel function J_0 centred at the drop position.

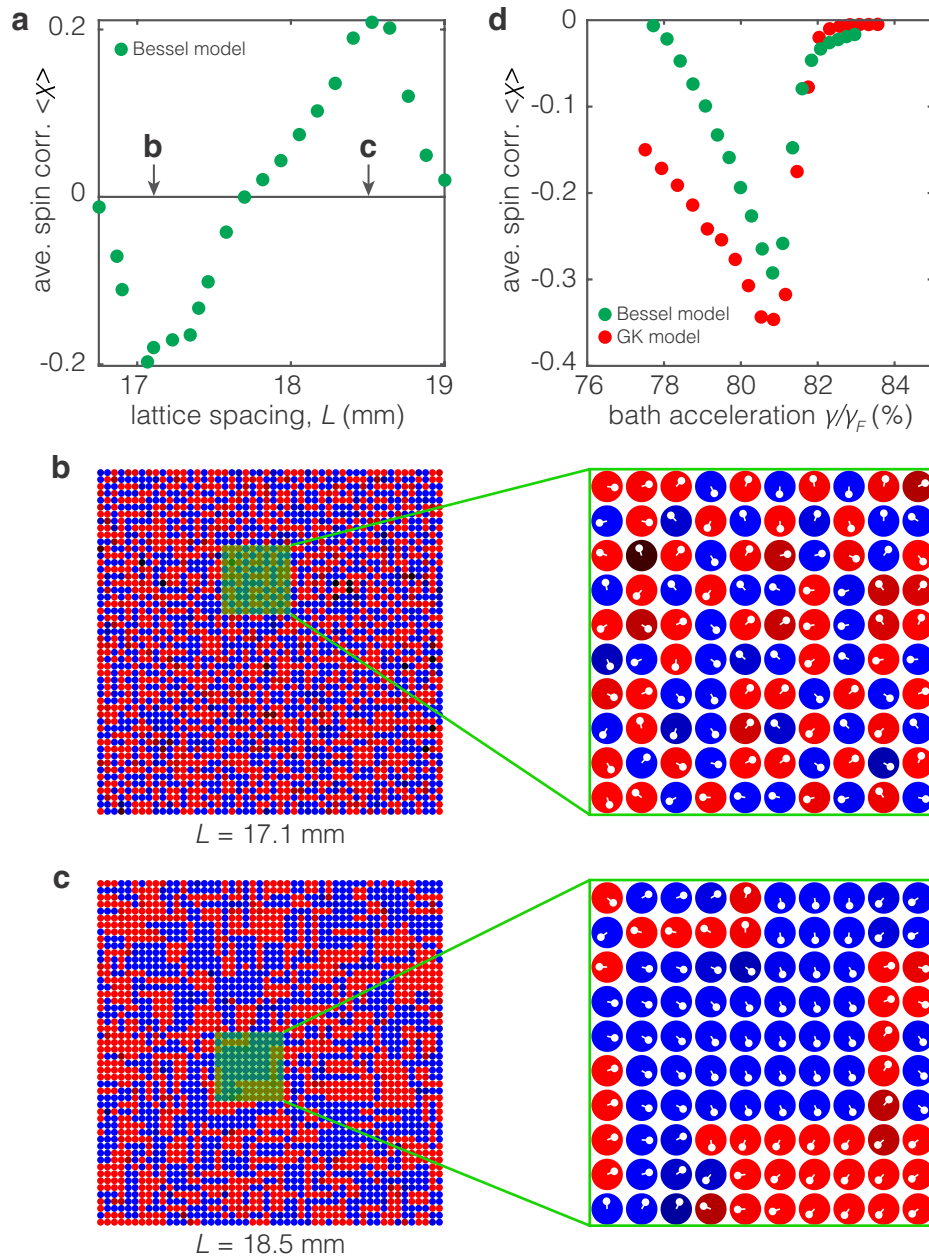


Extended Data Fig. 4 | Emergent order for varying lattice spacing. **a, b,** The dependence of the average spin correlation, $\langle \chi \rangle$ (**a**) and the mean phase difference, $\langle \Delta \phi \rangle$ (**b**) on the lattice spacing, L , as predicted by the Bessel model (equation (16)) with $\tau = 0.4$ s, $\omega_0 = 3.3$ s $^{-1}$, and $\mathcal{F} = 70$ s $^{-2}$. The average droplet-induced wave field, which is approximated by a Bessel function $J_0(k_F L)$, centred in the neighbouring well at $L = 0$, is provided for comparison in **a**. **c, d,** Dominant (**c**) and subdominant (**d**) synchronization modes for the corresponding sections (A–D) in **a, b**.



Extended Data Fig. 5 | Emergent order for varying bath acceleration.

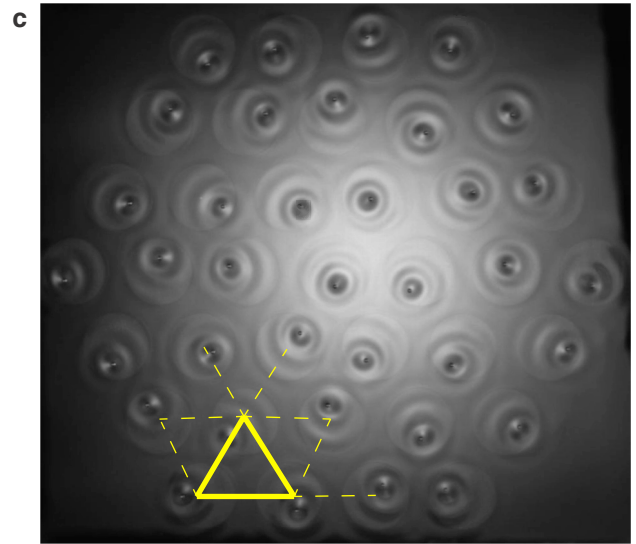
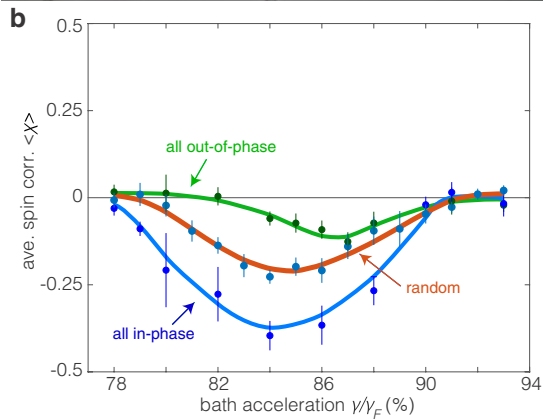
Comparison of the experimentally observed average spin correlation, $\langle \chi \rangle$, with the predictions of the Bessel model (equation (16)) and the generalized Kuramoto model (equation (23)). Solid lines are fits resulting from smoothing the piecewise linear plot given by connecting the points. Bessel model parameters: $L = 17.7$ mm, $r = 1.8$ mm, $\lambda_F = 2\pi/k_F = 5.1$ mm. The interaction parameter \mathcal{F} is varied across the range $70 < \mathcal{F} < 130$ s⁻² and transformed back to γ/γ_F using the relation from Extended Data Table 1. To simplify the simulations, we fix the relaxation time to be $\tau = 0.1$ s and the natural angular frequency to be $\omega_0 = 3.3$ s⁻¹, values consistent with experimental observation (Fig. 1c). The effective walker mass is set to $m_w = 1.65m$, in line with prior work⁶¹. GK model parameters: α is varied over the range $8.5 < \alpha < 15$ s⁻², while maintaining $\beta < 0$ and a constant ratio $|\beta/\alpha| = 0.3$. By dividing the expressions for α and β in equations (25), (26) by a factor of two, in accordance with the mismatch between the GK and Bessel models discussed in Supplementary Fig. 3, the minimum $\langle \chi \rangle$ predicted by the GK model emerged in the vicinity of γ_c .



Extended Data Fig. 6 | Emergent order in large 2D square lattices.

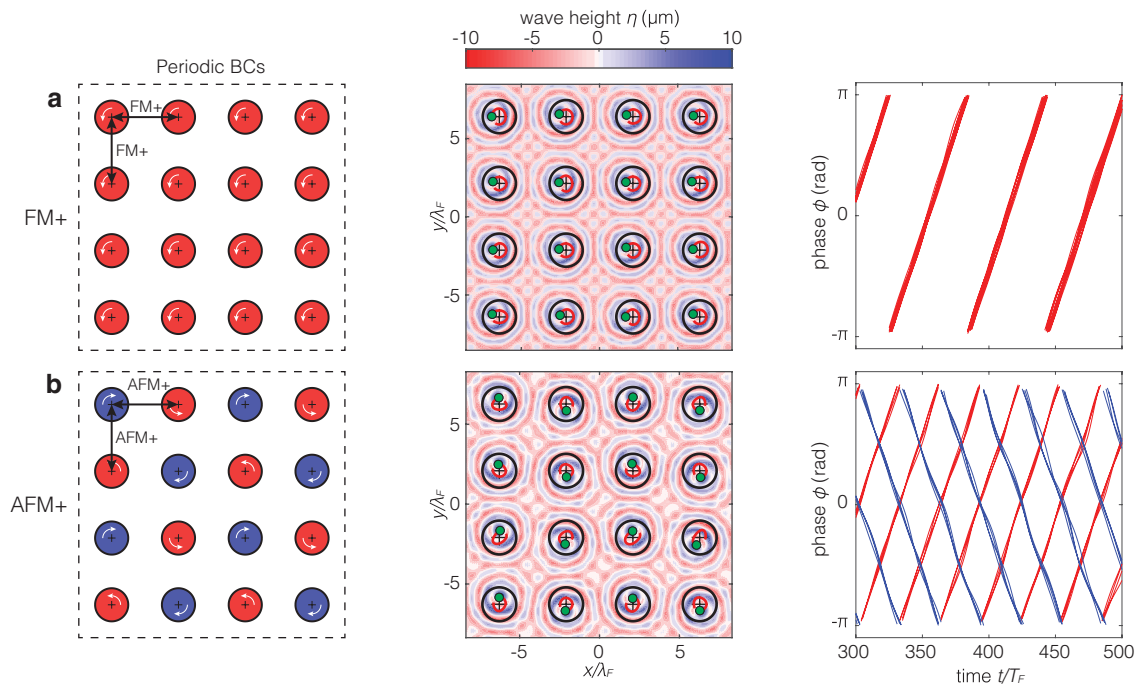
Simulations of the Bessel model (equation (16)) and the generalized Kuramoto model (equation (23)) for a 50×50 square lattice demonstrate the emergence of antiferromagnetic and ferromagnetic order in 2D for various lattice spacings and bath accelerations. **a**, The lattice spacing determines the emergent antiferromagnetic (ADM₊) or ferromagnetic (FM₊) order in a manner predicted by our reduced theory (equation (24)). **b, c**, Specifically, preferred in-phase rotation between neighbouring pairs can be clearly observed in the antiferromagnetic AFM₊ (**b**), and ferromagnetic FM₊ (**c**) regimes. We note that **b** and **c** correspond to simulations of the Bessel model with the spacings

indicated on **a, d**. The emergent in-phase antiferromagnetic order (AFM₊) as a function of bath acceleration. Bessel model parameters in **a**: $\tau = 0.1$ s, $\mathcal{F} = 72$ s⁻², $16.8 \leq L \leq 19$ mm, $\omega_0 = 3.3$ s⁻¹, and $\lambda_f = 4.95$ mm. Bessel model parameters in **d** are the same as in **a**, but with $L = 17.1$ mm and the interaction parameter varies across the range $65 \leq \mathcal{F} \leq 85$ s⁻², which is transformed back to γ/γ_f using the relation from Extended Data Table 1. GK model parameters in **d**: α is varied over the range $9.5 < \alpha < 13$ s⁻² while maintaining $\beta < 0$ and a constant ratio $|\beta/\alpha| = 0.07$, $\tau = 0.2$ s and $\omega_0 = 3.3$ s⁻¹. In all cases, each data point results from averaging 50 simulations of 600 s each, to ensure statistical significance.



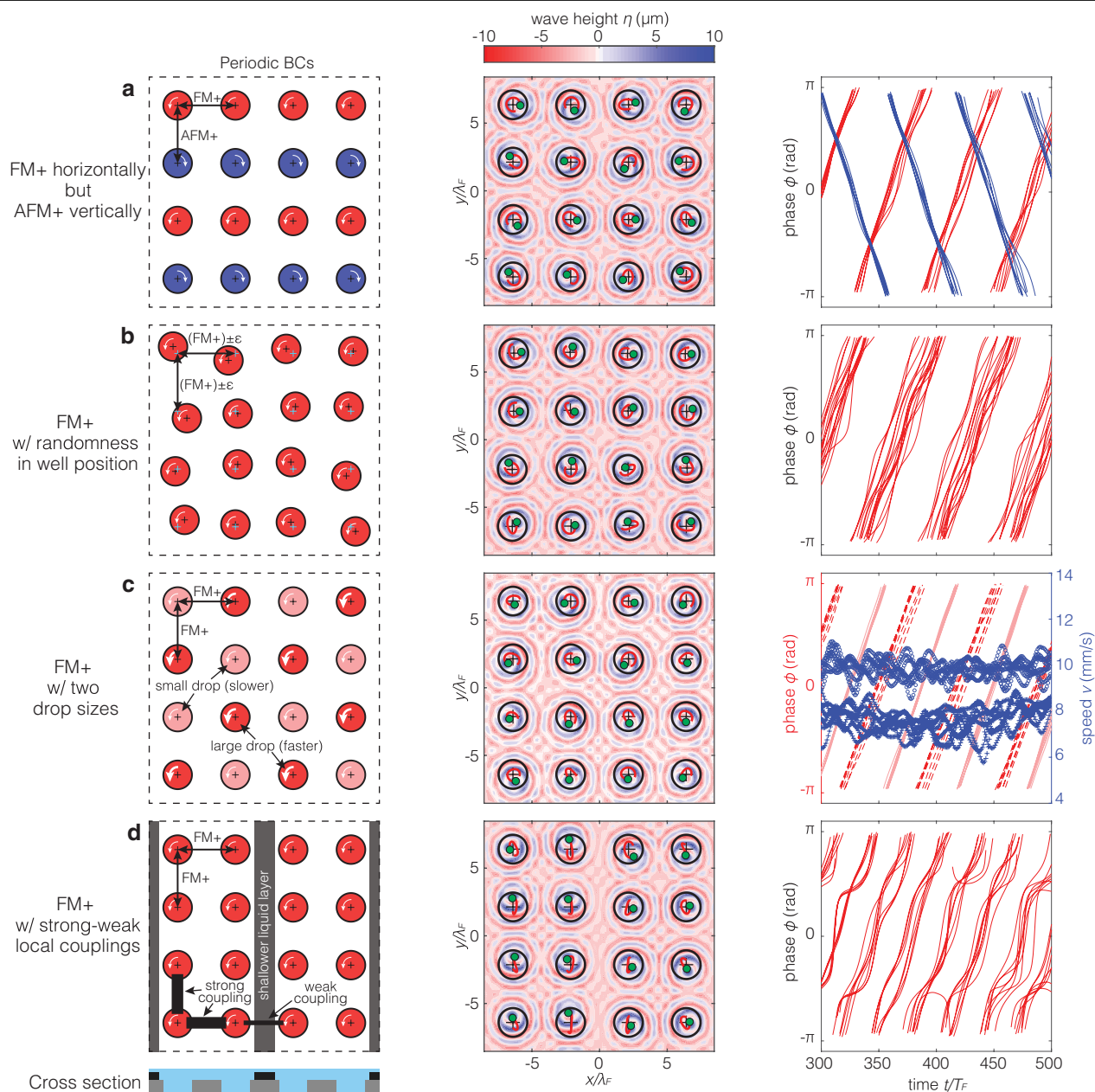
Extended Data Fig. 7 | Emergent order for different vertical bouncing synchronizations and lattice geometries. **a**, Oblique view of a 2D spin lattice where the walker in the centre is bouncing vertically in-phase and out-of-phase with its left and right neighbours, respectively. **b**, Average spin correlation for lattices with the same geometry as those described in Fig. 1 when the walkers all bounce in phase (blue, result presented in text), out of phase (green), or have randomly distributed bouncing phases (red). Vertically in-phase pairs promote in-phase orbital antiferromagnetic order (AFM.), whereas vertically

out-of-phase pairs promote out-of-phase orbital antiferromagnetic order (AFM.). A random distribution of vertical phases thus leads to competing orbital synchronization modes, which has an effect on the emergent spin correlation. Solid lines are fits resulting from smoothing the piecewise linear plot given by connecting the points. **c**, Triangular HSLs with a lattice spacing tuned to promote antiferromagnetic order can be used to investigate frustration effects.



Extended Data Fig. 8 | Emergent collective order in simulations. Simulations of square HSLs with the theoretical model developed previously⁶⁸ is used to explore collective order in 2D. **a, b**, For appropriate lattice spacings,

in-phase ferromagnetic order FM, **(a)** and in-phase antiferromagnetic order AFM, **(b)** are simulated. Left, schematic; middle, wave field and walker's trajectories; right, time evolution of the orbital phases.



Extended Data Fig. 9 | Model tunability. Proof-of-concept simulations performed with the model developed previously⁶⁸ illustrate the tunability and potential for future research of HSLs. Left, schematic; middle, wave field and drop trajectories; and right, orbital phase evolution. **a**, An HSL tuned to promote FM_x along the horizontal direction, but AFM_x across vertical pairs.

b, FM_x lattice geometry with a random vertical and horizontal shift $\pm\epsilon$ in the position of each well. **c**, FM_x lattice geometry with two drop sizes (and so, two walker speeds). **d**, FM_x lattice geometry with coupling strength controlled locally through the thickness of the liquid layer.

Article

Extended Data Table 1 | Model parameters and physical variables for HSLs

Variable	Description
$\sigma, \mu, \rho, \nu = \mu/\rho, \nu_e, \mu_a$	Liquid surface tension, dynamic viscosity, density, kinematic viscosity, effective kinematic viscosity, air viscosity
m, D_d, R_d	Droplet mass, droplet diameter, droplet radius
D, L, r	Well diameter, center-center separation, orbital radius
γ, f	Bath forcing acceleration, frequency
$k_F, T_F = 2/f, \gamma_F$	Faraday wavenumber, period and threshold
$T_D = (\nu_e k_F^2)^{-1}, T_M = \frac{T_D}{(1-\gamma/\gamma_F)}$	Viscous decay time, wave-decay memory-time [36]
$C = 0.17, \mathcal{D} = Cmg\sqrt{\frac{\rho R_d}{\sigma}} + 6\pi R_d \mu_a$	Drag coefficient, time-averaged horizontal drag coefficient [36]
$F = \sqrt{\frac{\nu_e T_F}{2\pi}} \frac{(mgk_F^2 R_d)^2}{3\sigma k_F^2 + \rho g} \sin \Phi, \sin \Phi$	Wave-force coefficient, phase parameter [36]
$m_w = m \left(1 + \frac{F k_F T_M^2}{2m} \right)$	Effective walker mass
$D_R = \mathcal{D} \left(\frac{F k_F T_M^2}{2T_F \mathcal{D}} - 1 \right), \tau = \frac{m_w}{D_R}$	Rayleigh-drag strength, Relaxation time
$u_0^2 = \frac{8}{3k_F^2 T_M^2} \left(\frac{F k_F T_M^2}{2T_F \mathcal{D}} - 1 \right), \omega_0 = \frac{u_0}{r}$	Free walking speed, angular velocity
$\mathcal{F} = \frac{F T_M}{T_F m_w r}$	Interaction force coefficient